Internal structures and dating of non-sulphide Zn deposits 5 using rock magnetism: insights from the Moroccan High Atlas

Nicolas Charles, Flavien Choulet, Stanislas Sizaret, Yan Chen, Luc Barbanson, Aomar Ennaciri, Lakhlifi Badra, Yannick Branquet

HAL Id: insu-01164517
https://insu.hal.science/insu-01164517

Submitted on 26 Jun 2015

Internal structures and dating of non-sulphide Zn deposits using rock magnetism: Insights from the Moroccan High-Atlas

Nicolas CHARLES[1,*], Flavien CHOULET[2], Stanislas SIZARET[3], Yan CHEN[3], Luc BARBANSON[3], Aomar ENNACIRI[4], Lakhlifi BADRA[5], Yannick BRANQUET[3].

1: Bureau de Recherches Géologiques et Minières (BRGM-French Geological Survey), Orléans, France

2: Université de Franche-Comté, UMR-CNRS 6249 Chrono-Environnement, Besançon, France

3: Institut des Sciences de la Terre d'Orléans, UMR 7327-CNRS/Université d'Orléans/BRGM, Orléans, France

4: Groupe Managem, Casablanca, Morocco

5: Université Moulay Ismaïl, Meknès, Morocco

Abstract

The renewal of interest in Zn-Pb non-sulphide ores has been induced by mineral processing improvement and leads to new exploration and mining projects in the world. Although the mineralogy is often precisely known, and despite several studies linking ore deposition to regional tectonics, absolute dating of non-sulphide stages is rare and structure of ore bodies was largely disregarded. Geochronological data from non-sulphide ores are essential to timely constrain alteration episodes and to insert supergene ore genesis in the climate and tectonic evolution of the metallogenic province. The access to internal organisation of ore could reveal post-mineralization episodes related to supergene evolution. Thus, a rock magnetism study combining Anisotropy of Magnetic Susceptibility (AMS) and palaeomagnetism was performed on four non-sulphide deposits from the Moroccan High-Atlas. AMS generally shows similar horizontal magnetic fabrics for ores and the clayey and carbonaceous internal sediments filling karstic cavities. The palaeomagnetic directions of ores and internal sediments are compatible and the calculated poles are consistent with the last 30

Ma of the Africa Apparent Polar Wander Path, with an upper age at 0.78 Ma. The proposed three-step scenario is placed within the evolution of the Moroccan High-Atlas belt. Deposition of primary sulphides is contemporaneous with opening of the Tethyan and Atlantic oceans. During the Tertiary, intracontinental deformation gave rise to the High-Atlas fold-and-thrust belt and to regional uplift. Finally, Zn-Pb sulphides, hosted in carbonates experienced oxidation under an arid climate to form karst-related Zn-Pb non-sulphide ores. These promising results pave the way for an efficient method to constrain the internal fabrics and age of Zn supergene deposits.

Key-words: non-sulphide Zn deposit, AMS, palaeomagnetism, dating, High-Atlas, Morocco.

*Corresponding author: n.charles@brgm.fr

1. Introduction

Non-sulphide zinc ores, also called "calamines" or "zinc oxides" were the main sources of zinc metal until the end of the nineteenth century (e.g. Large 2001; Boni et al. 2003; Hitzman et al. 2003). New processing technologies, such as hydrometallurgical acid-leaching, solvent extraction (SX) and electro-winning techniques (Cole and Sole 2002; Gnoinski 2007; Hosseini 2008), recently lead to a regain of interest in non-sulphide Zn-Pb ores with exploration and mining projects in Iran (Daliran et al. 2009; 2013), Namibia (Borg et al. 2003), Zambia (Terraciano 2008), Turkey (Santoro et al. 2013) and Peru (Boni et al. 2009). In non-sulphide Zn ores, zinc occurs as a major component of carbonates (smithsonite), silicates (willemite), hydrated minerals (Zn-clays, hemimorphite, hydrozincite) and minor phases listed in Hitzman et al. (2003). Based on physico-chemical conditions for

mineral occurrence, hypogene and supergene deposits have been distinguished (Heyl and Bozion 1962; Large 2001; Hitzman et al. 2003). Only supergene deposits will be discussed in this article.

During the last decade, many efforts have been made on understanding metallogeny of non-sulphide zinc deposits. Research has focused on describing the different zinc-bearing minerals (e.g. Borg et al. 2003; Boni et al. 2009; Daliran et al. 2009) and identifying the physico-chemical conditions they were formed (e.g. Boni et al. 2003; Reichert and Borg 2008; Choulet et al. 2014). Although the succession of mineral assemblages is often known in detail, absolute dating of non-sulphide stages is rare and limited to particular geochronometers such as Rb/Sr on willemite or clay (Schneider et al. 2008), U/Th-He on zinc vanadate (Boni et al. 2007) or Ar/Ar on zinc-lead manganese oxide (Groves et al. 2003). Obtaining geochronological data from non-sulphide mineralogical assemblage are essential to timely constrain oxidation episodes and to insert supergene ore genesis in the climate and tectonic evolution of the metallogenic province. In addition, despite several studies linking ore deposition to regional tectonics (Borg 2003; 2009), the structure of ore bodies was largely disregarded, as a consequence of the intricate supergene processes involved in karst-related deposits, where multiple weathering episodes and evolution of the hydrodynamics have contributed to successive chemical and mechanical reworking, respectively (Boni et al. 2003). Therefore, macroscopic and microscopic observations are often not sufficient to decipher the ore internal structure. To image these fabrics, it is possible to recourse to magnetic properties of minerals and especially to anisotropy of the magnetic susceptibility (AMS). This tool may provide information on the internal organisation of ore and can be used to reveal post-mineralization episodes related to supergene evolution (e.g. Essalhi et al. 2009). When geochronometer minerals are absent, the approach of palaeomagnetism can be also useful to indirectly constrain the age of mineralization. These methods have been successfully applied

3

77   to various types of deposits like VMS gossan (Essalhi et al. 2011), MVT (Symons et al. 1996;

78   2002), and iron laterites (Théveniaut and Freyssinet 1999; 2002; Théveniaut et al. 2007;

79   Ricordel-Prognon et al. 2010). Boni et al. (2005) attempted dating of non-sulphide Zn-Pb ores

80   of SW Sardinia (Italy) by palaeomagnetism. Despite scarce sampling and non-conclusive

81   results, the authors suggested that this method can be effective to constrain the timing of

82   oxidation in supergene-enriched ores, representing an interesting methodological challenge

83   with multiple possible targets throughout the world.

84   This contribution aims at showing that rock magnetism properties may be used to

85   constrain age and geometry in supergene ore deposits, with the example of the Moroccan zinc

86   non-sulphide deposits. The Moroccan High Atlas is an intracontinental Cenozoic belt that

87   exposes numerous supergene Zn non-sulphide deposits hosted in the Lower Jurassic

88   limestone (**Figure 1**). Choulet et al. (2014) studied the mineralogical assemblage of six

89   deposits and identified a direct replacement of Zn-Pb sulphides by carbonates and silicates,

90   accompanied by precipitation of Zn non-sulphide minerals in cavities with internal karstic

91   sedimentary filling. Based on field observations, they proposed that formation of the non-

92   sulphide ore is coeval with Atlas deformation and uplift during the Cenozoic. Therefore this

93   area represents a good target to use palaeomagnetism to timely constrain the supergene

94   oxidation episodes. We have selected four localities (Aït Labbès, Toulal, Beni Tajite and

95   Tadaghast; **Figure 1**) and collected samples from both veins of non-sulphide Zn ore and

96   cavities filled by internal karstic sediments. After a careful study of the mineralogy to identify

97   the magnetic carriers, we present AMS and palaeomagnetism results that allow us to discuss

98   the internal structure of the mineralized body and its age in the general framework of the

99   Atlas tectonic and climate evolution.

100

101   **2. Geological and metallogenetic setting**

102

2.1. The Moroccan High-Atlas

104

The Atlas Mountains is an intracontinental orogen, WSW-ENE trending mountain belts, extending from Morocco to Tunisia (e.g. Frizon de Lamotte et al. 2009 and references therein; **Figure 1a**). The Moroccan High-Atlas is composed of Mesozoic to Cenozoic sedimentary rocks overlying on a Precambrian to Palaeozoic basement (**Figures 1b and 1c**), deformed during the Variscan orogeny (Mattauer et al. 1977; Piqué and Michard 1989). According to Laville and Piqué (1991), inheritance of Palaeozoic structures largely constrains the geometry of the Mesozoic rifting episode related to the opening of the Tethys and the Atlantic Ocean. The sedimentary pile comprises from bottom to the top: 1) Triassic detrital rocks, evaporites (du Dresnay 1988; Piqué 1994) associated with mafic volcanics lava, 2) Lower to Middle Jurassic marl, limestone and calcareous turbidite, and 3) upper Middle Jurassic continental red beds (Charrière et al. 2005) with contemporaneous magmatism (Brechbühler et al. 1988; Laville and Piqué 1992). Sedimentation resumed with Cretaceous red sandstone and limestone deposits. The Late Cretaceous carbonate platform marks a short but major Late Cenomanian-Turonian transgression event (Haddoumi et al. 2008), since continental sedimentation is recorded again at the end of Cretaceous, during the Palaeocene (Charrière et al. 2009) and until the mid-Eocene (Herbig and Trappe 1994).

Presently, the Moroccan High-Atlas exhibits a fold-and-thrust bulk architecture that results from inversion tectonics of the former Mesozoic extensional basins, controlled by NE-SW trending normal faults (Laville et al. 2004; Frizon de Lamotte et al. 2008). The NE-SW strike of the faults is slightly oblique to the general ENE-WSW trend of the belt (**Figure 1a**). Lower to Middle Jurassic strata are found in the wide and open synclines, while anticlines are comparatively narrow and are underlined by thick Lower Jurassic limestone ridges (**Figure**

127 **1c**). Locally, the anticline hinges are affected by thrusting, exposing the underlying Triassic

128 strata that form the décollement layer. The formation of the intracontinental belt in the

129 Moroccan High-Atlas (Mattauer et al. 1977) has been facilitated by the inherited crustal

130 weaknesses due to Mesozoic rifting. Although the chronology of faulting and uplift is still

131 disputed, inversion tectonics of the Triassic to Jurassic normal faults occurred between

132 Eocene and Quaternary, with alternation of quiet and active periods of uplift (Frizon de

133 Lamotte et al. 2009). While compression chiefly occurs at the Lutetian-Bartonian transition

134 (ca. 40 Ma), a secondary Pleistocene episode has caused the present topography of the range.

135   The Lower Jurassic carbonate massif of the Moroccan High Atlas has experienced

136 intense karstification driven by 1) the tectonic structures relative to Tertiary tectonics, and 2)

137 the lithology, with a preferred development of karst network in reef limestone and dolostone

138 (Couvreur, 1978). Several episodes of karst development have been recorded in the literature:

139 1) an early stage (Lower Jurassic) coeval with sulphide deposition is recorded at Beni Tajite

140 deposit (Choulet et al. 2014), a Cretaceous event during a major emersion phase (Subra,

141 1980), post-Eocene to Mio-Pliocene episodes related to the Atlas tectonics and exhumation of

142 the Jurassic rocks (Bouchaou, 1988), and Pliocene to Quaternary evolution (Nicod, 1997)

143 driven by the reactivation of Atlas faults.

144

145 2.2. Non-sulphide Zn-Pb deposits of Moroccan High-Atlas

146

147   The numerous Zn-Pb ore deposits in Northern Africa belong to the Zn-Pb province of

148 the circum-Mediterranean Sea and Alpine Europe (Rouvier et al. 1985), a wide area of

149 economic interest for the extraction of base metals (Emberger 1969; Popov 1968; Decrée et

150 al. 2008; 2010; Bruyère et al. 2010; Jemmali et al. 2011). In the Moroccan High-Atlas, Zn-Pb

151 ore deposits occur throughout the belt (**Figure 1b**). Two main metallogenic periods have been

152   recognized for Zn-Pb sulphide ore deposition (Mouguina 2004): (1) the Lower Jurassic

153   period, with stratabound lenses of Zn-Pb-Fe sulphides considered as syngenetic (Agard and

154   du Dresnay 1965; Emberger 1965; Bazin 1968; Auajjar and Boulègue 1999); (2) the Middle

155   Jurassic (i.e. Dogger) period, characterized by Cu-Ni and Zn-Pb ore deposits spatially and

156   temporally associated to mafic magmas, and to reactivated faults (Caïa 1968; Chèvremont

157   1975).

158   In the Moroccan High-Atlas, Zn-Pb mineralization often consists of non-sulphide zinc

159   ores, locally called "calamines" (Ovtracht 1978), which are considered to result from the

160   supergene alteration of a primary carbonate-hosted sulphide protore (Agard and du Dresnay

161   1965; Bazin 1968; Leblanc 1968; Mouguina 2004). The origin of primary sulphides (Sedex or

162   MVT types) is not clearly established yet and is beyond the scope of this paper. Based on

163   field and mineralogical studies of six non-sulphide Zn-Pb deposits, Choulet et al. (2014)

164   recently published a new model to explain the formation of Moroccan High-Atlas non-

165   sulphide ore deposits. They recognized two superimposed stages of weathering, following the

166   formation of the protore sulphides (themselves more or less coeval with deposition of Lower

167   Jurassic host limestone):

168   - (1) early supergene weathering with formation of Zn-Pb carbonates and iron oxi-

169   hydroxides,

170   - (2) late supergene weathering with deposition of Zn-carbonates, Zn-silicates and

171   hydrated phases.

172   The proposed scenario falls within the tectonic evolution of the Moroccan High Atlas

173   belt. Deposition of primary sulphides is contemporaneous with opening of the Tethyan and

174   Atlantic oceans. During the Tertiary, intracontinental deformation has given rise to the High

175   Atlas fold-and- thrust belt and to regional uplift. As a result, Zn–Pb sulphides, hosted in

176   carbonates experienced oxidation under an arid climate to form karst-related Zn–Pb non-

7

177 sulphide ore bodies. Our good understanding of processes involved and the well-established

178 chronology allow us to study, rock magnetism to constrain the ore body structure and its

179 formation age by means of magnetic fabrics and palaeomagnetism, respectively. Despite this

180 complex weathering evolution, iron-bearing phases representing the main magnetic carriers,

181 are formed during the early supergene event and not reworked by the late one, apparently

182 preventing remagnetization.

183

184 2.3. The Tadaghast, Aït Labbès, Toulal and Beni Tajite ore deposits

185

186 In this study, four occurrences and deposits have been investigated: Tadaghast, Aït

187 Labbès, Toulal and Beni Tajite (**Figure 1b**). The geological setting has been extensively

188 studied by Choulet et al. (2014). Only a brief outline of macroscopic and microscopic

189 observations is provided here (Figures 2 and 3), and the reader can refer to Choulet et al.

190 (2014) and references therein for a more detailed description.

191 In the field, non-sulphide Zn-Pb deposits are often associated to tightly faulted

192 anticlines (**Figure 2a**), except for the tabular series that hosts the Beni Tajite ore deposit

193 (Agard and du Dresnay 1965). Non-sulphide ores are always hosted in Lower Jurassic

194 limestone formed in a reefal or para-reefal environment commonly close to the transition

195 from the platform to the deep sea (du Dresnay 1979; Leblanc 1968). Mineralized system is

196 associated to a karst-related network formed after tectonic features and exposing dissolution

197 cavities in the limestone, as well exemplified at Toulal and Aït Labbès sites (**Figures 2b, 2c**

198 **and 2d**).

199 The protore mainly consists of stratabound lenses of primary sulphides (galena,

200 sphalerite and pyrite; **Figure 3a**) and massive white calcite. Superimposed supergene

201 oxidation includes the formation of non-sulphide Zn-Pb minerals and iron oxi-hydroxides

202   (e.g. smithsonite, hemimorphite, hydrozincite, goethite, hematite; **Figures 2e and 2g**). Two

203   successive types of non-sulphide ores have been observed all over the studied sites (Choulet

204   et al. 2014; **Figures 2h and 2i**):

205   - a red ore (locally called red calamine) composed of the iron oxi-hydroxides-

206   smithsonite association (**Figures 2h, 3b and 3c**); in all samples dissolved pyrite are replaced

207   by zoned goethite and hematite (Choulet et al. 2014).

208   - a "grey to white ore" (locally called grey or white calamine) superimposed on the red

209   type or precipitated in karst cavities with limited metal transport (**Figures 2i and 3d**). It is

210   worth to notice that no iron oxi-hydroxides are involved in this second stage.

211   Besides, the development of the karst network within limestone host-rocks implies

212   internal sedimentation, as evidenced by horizontally bedding within up to 10 meters scale

213   cavities (**Figure 2f**). Locally, the horizontal bedding is disturbed due to either sedimentary

214   processes or post-deposition tectonics. Although interference between karst formation and

215   supergene evolution of ore may occur, internal sediments are usually Zn-poor (grading 4-5

216   ZnO wt.%, Choulet et al., 2014), and mainly made up of marl and calcareous shale including

217   clasts of calamine and iron (hydr-)oxides (**Figures 3e and 3f**). Laminated internal sediments

218   display micrometric to centimetric alternations of banded calcite and matrix-supported beds

219   including detrital residual clays and a mix of carbonate and iron oxides coeval with the karst

220   development (**Figure 3e**). Alternatively, clast-supported sediments present sub-rounded

221   fragments of iron oxides and calcite. These clasts are cemented by secondary massive or

222   drusy calcite (**Figure 3f**). Finally, a synoptic paragenetic sequence can be proposed for all the

223   studied deposits as shown in **Figure 3g**.

224

225   **3. Methods and sampling**

226

9

3.1. Sampling strategy

Using a portable gasoline drill, a total of 157 cores has been collected from non-sulphide Zn ore (98 cores), internal sediment (39 cores) and host Lower Jurassic limestone (20 cores) in four localities (**Figure 1b**): Aït Labbès (AL), Toulal (T), Beni Tajite (BT) and Tadaghast (TA). At Aït Labbès, 51 cores (38 of non-sulphide Zn ore, 9 of internal sediment and 4 of host limestone) were sampled in a bunch of N60°-trending cavities at 3 sites (i.e. AL1, AL2 and AL3; **Figures 4a, 4b and 4c**). At the Toulal prospect, 47 cores (15 of non-sulphide Zn ore, 22 of internal sediment and 10 of host limestone) were collected at 3 sites (i.e. T1, T2 and T3; **Figures 4d, 4e and 4f**). At Beni Tajite, 30 cores were drilled in grey non-sulphide Zn ore (i.e. BT1 and BT2; **Figure 4g**). Finally, 29 cores (15 of non-sulphide Zn ore, 8 of internal sediment and 6 of host limestone) were collected at Tadaghast, in the currently exploited galleries with two sites corresponding to E-W sub-vertical and stratabound veins (TA1 and TA2, respectively; **Figures 4h and 4i**). Cores have been oriented with both magnetic and sun compasses, when it was possible, to correct the local magnetic field anomalies. The average difference between magnetic and solar declinations is about 5.8°. In additions, two blocks oriented on field have been collected at Toulal (T3) and Tadaghast (TA6) and further drilled in lab. Then, cores were cut into standard specimens of 22 mm in length and 25 mm in diameter for both AMS and palaeomagnetic measurements.

3.2. Methods and analytical procedure

3.2.1. Anisotropy of Magnetic Susceptibility (AMS)

251　　　　　　Magnetic susceptibility (K) is defined by K=M/H where M is the induced

252　　　magnetization of the material and H, the inducing magnetic field (see Rochette et al. 1992 for

253　　　details). The susceptibility is described as a symmetric second rank tensor, which can be

254　　　depicted by an ellipsoid defined by three orthogonally oriented axes: K_1, K_2 and K_3 (with

255　　　$K_1 \geq K_2 \geq K_3$). K_1 and K_3 are considered to be the magnetic lineation and the pole of the

256　　　magnetic foliation, respectively. Thus, the Anisotropy of Magnetic Susceptibility (AMS) is

257　　　the property of a material whereby a given magnetic field applied in different directions

258　　　produce variable intensities of induced magnetization. A number of parameters can be

259　　　calculated to characterize the AMS ellipsoid, but the most widely used are the mean magnetic

260　　　susceptibility (K_m), the corrected anisotropy degree (P_J), and the shape parameter (T) (Tarling

261　　　and Hrouda 1993). In the case of low susceptibility, these parameters and especially the P_J

262　　　values should be used with caution, as it has not been corrected from the diamagnetic

263　　　component (not measured in this study). The AMS is a physical property of rocks that define

264　　　the magnetic fabric and is used for characterizing internal rock textures and structures (e.g.

265　　　Hrouda 1982; Sizaret et al. 2003; Charles et al. 2009; 2012; Essalhi et al. 2009).

266

267　　*3.2.2. Palaeomagnetism*

268

269　　　　　　Palaeomagnetism relies on the study of the magnetic remanence involved by

270　　　ferromagnetic *s.l.* minerals present in the rocks. During sediment deposition, or syn-

271　　　diagenetic precipitation, these minerals may record the Earth magnetic field that can be

272　　　preserved through time and be used for indirect age constraints (e.g. Van der Voo 1993).

273　　　Dating ore deposition through palaeomagnetism, especially stratabound, disseminated and

274　　　massive sulphide ore deposits has beneficiated of major advances since last two decades (e.g.

275　　　Symons et al. 1996; 2002; Symons and Stratakos 2000; Leach et al. 2001; Bradley and Leach

2003; Pannalal et al. 2008). Palaeomagnetism can be also used to establish the timing of weathering, with characteristic example of laterite profiles or gossans (Théveniaut and Freyssinet 1999; 2002; Théveniaut et al. 2007; Ricordel 2007; Ricordel-Prognon et al. 2010; Essalhi et al. 2011). Hence, the absence of time constraints for non-sulphide Zn-Pb deposits of Moroccan High-Atlas could be overcome using palaeomagnetism coupled with field observations and a detailed mineralogical study (Choulet et al. 2014).

3.2.3. Technical procedure

Prior to carry out the AMS and palaeomagnetic studies, magnetic mineralogy has been investigated by four techniques: (1) X-ray diffraction (INEL XRM3000 diffractometer in transmission mode coupled to an INEL CPS 120 curved position sensitive detector), (2) thermomagnetic measurements (AGICO CS3 coupled with AGICO KLY3-S Kappabridge apparatus), (3) Isothermal Remanent Magnetization (IRM; AGICO JR5-A spinner magnetometer coupled with ASC Scientific IM-10-30) and (4) bulk magnetic susceptibility (AGICO KLY3-S Kappabridge apparatus). We have further measured the Anisotropy of Magnetic Susceptibility using AGICO KLY-3S Kappabridge apparatus and the average orientation of the three principal ellipsoidal axes of AMS for groups of samples was computed with ANISOFT software using Jelinek's statistics (Jelinek 1981). Both thermal and Alternative Field (AF) demagnetizations have been carried out by laboratory-built furnace and AGICO LDA-3 demagnetizer, respectively. Step heating includes an average of ten steps between natural remanent magnetization (NRM) and 680°C. The magnetic remanence was measured using AGICO JR5-A spinner magnetometer to remove recent viscous remanent magnetization components from the magnetic remanence of specimens. The directions of the magnetic remanence were isolated by principal component analysis (Kirchvink 1980) and

301 mean directions were computed by spherical statistics (Fisher 1953) using palaeomagnetic

302 software packages of Cogné (2003) and R. Enkin (unpublished). All measurements were

303 performed at Institut des Sciences de la Terre d'Orléans (ISTO).

304

305 **4. Results**

306

307 4.1. Magnetic mineralogy of non-sulphide Zn-Pb deposits and internal karstic sediment

308

309   X-ray diffraction pattern reveals that red ore is composed of goethite, calcite and

310 smithsonite (**Figures 5a and 5b**), whereas grey calamine only includes smithsonite (**Figure**

311 **5c**). For internal sediments, goethite, calcite and quartz have been identified (**Figure 5d**), and

312 the large bulge at small θ values attests for a significant clay minerals component. These

313 results are in accordance with field and microscopic observations (**Figures 2 and 3**).

314   Bulk magnetic susceptibility intervals for each lithology are plotted in **Figure 6**. The

315 majority of ore samples present magnetic susceptibilities lower than 200.10^{-6} SI and up to

316 800.10^{-6} SI suggesting the contribution of ferromagnetic *s.l.* minerals. The magnetic

317 susceptibilities of internal sediment and host limestone samples are weakly positive (below

318 100.10^{-6}SI), suggesting that both rock types include paramagnetic minerals, with a small

319 amount of ferromagnetic *s.l.* minerals. In addition, several ore samples (mainly grey ore)

320 display negative values of bulk magnetic susceptibility, suggesting the dominance of

321 diamagnetic minerals, like iron free carbonate.

322   Isothermal remanent magnetization (IRM) was carried out on 11 representative

323 samples (ores and internal sediments), and results are presented in **Figure 7**. For this

324 technique, samples are magnetized in an increasing direct magnetic field and the resulting

325 IRM saturation pattern is typical of the different ferromagnetic *s.l.* minerals. The red ore and

internal sediments samples from Aït Labbès, Toulal and Tadaghast show similar patterns (**Figures 7a, 7b and 7d**). Samples exhibit a first rapid increase of the induced field at weaker applied fields leading to consider the presence of low-coercive minerals (e.g. magnetite). Then, a lack of magnetic saturation at an applied magnetic field up to 1.4 T is observed, which is typical of high-coercive minerals, such as goethite and/or hematite. For the grey ore of Beni Tajite (**Figure 7c**), the saturation below 150 mT indicates the occurrence of low-coercive minerals (e.g. magnetite). The magnitude of remanence confirms the low concentration of magnetic minerals.

Thermal monitoring of the magnetic remanence and the magnetic susceptibility (Curie temperature evaluation) are presented in **Figure 8**. For the red ore collected at Aït Labbès, Toulal and Tadaghast, thermomagnetic curves (**Figures 8a, 8b and 8c**) present two or three drops of the magnetic remanence at about 100-120°C, 300-350°C (only for samples AL2-3B and T2-11) and 580°C, corresponding to goethite, maghemite (titanomaghemite) and magnetite Curie temperatures, respectively. These observations are partially confirmed by thermal magnetic measurements with magnetic susceptibility dropping at around 300-350°C and 580°C (**Figure 8d**). The presence of hematite, observed under microscope (Choulet et al. 2014) is probable, as magnetic remanence and susceptibility values continue to slightly drop beyond 580°C (**Figures 8a to 8d**). For internal sediments, the evolution of the magnetic remanence with temperature is the same for each locality, with two drops at around 100-150°C and 580°C (**Figures 8e, 8f and 8g**), in accordance with the presence of goethite and magnetite. Minor hematite is also suspected by the slight drop at 580°C (especially for sample T1-17). This observation partially coincides with thermal magnetic measurements as magnetic susceptibility dropping up to 580°C is due to the magnetite Curie temperature (**Figure 8h**). As for the red ore, hematite is probably present owing to the pattern of magnetic remanence and susceptibility curves above 580°C (**Figure 8f**).

351

4.2. Magnetic fabric study (AMS)

353

At Aït Labbès, the AMS pattern is highly heterogeneous for red ore samples, with variable directions of the principal axes and broad error ellipses (**Figure 9a**). Nevertheless, magnetic foliation appears to be relatively steep and roughly parallel to the azimuth of the karst cavity (~N50°). For internal sediments, the magnetic foliation is well-defined and horizontal, with a weakly constrained E-W lineation. In the host limestone, the lineation presents a NW-SE trending and the magnetic foliation is slightly oblique, about 20°, a value close to the dip of the bedding (**Figure 4a**). Both ore and internal sediment samples present low values of the corrected anisotropy degree (P_J<1.01), without correlation with bulk susceptibility, except for high values of susceptibility (**Figure 9a**). The coexistence of positive and negative values of the shape parameter suggests that fabrics are both prolate and oblate. Conversely, in the host limestone, P_J value is higher than 1.01, whilst bulk susceptibility is very low; T value is positive and fabric is apparently oblate.

At Toulal, both ore and internal sediment samples present homogenous measurements of the AMS principal axes directions, with a well-defined horizontal foliation and poorly constrained WNW-ESE lineation (**Figure 9b**). As the host limestone is homogeneous for all three sites, AMS measurements have been compiled into one stereogram (**Figure 9b**). The fabric is quite well-defined and foliation exhibits a strong south-eastward dipping. In ore samples, positive and negative T values are observed, as well as a strong variability of the P_J parameter that is correlated with bulk susceptibility; the higher susceptibility is, the less the corrected anisotropy degree is. Conversely, only oblate fabrics are observed for internal sediments (positive T values), while P_J varies from 1 to 1.06 (**Figure 9b**).

375   The grey ore samples from Beni Tajite display a well-defined horizontal foliation and

376   NW-SE trending lineation (**Figure 10a**). The majority of T values are positive, suggesting a

377   dominantly oblate shape. Values of the corrected anisotropy degree are bracketed between

378   1.01 and 1.17, without correlation with bulk susceptibility.

379   As for Aït Labbès, the ore samples from Tadaghast display heterogeneous AMS

380   pattern, with variable directions of principal axes and large envelope error (**Figure 10b**). Both

381   positive and negative T values are observed, while P_J and bulk susceptibility values are

382   homogeneously weak. For the internal sediments, the fabrics are fairly defined with a

383   horizontal foliation and NW-SE lineation (**Figure 10b**). AMS parameters show P_J values

384   comprised between 1.02 and 1.04 with a bulk magnetic susceptibility yielding from 300 to

385   900.10^{-6} SI. Finally, the fabrics of the host limestone are quite well-defined with an steeply

386   inclined foliation (up to 70°). The P_J parameter varies from 1.01 to 1.04, while bulk

387   susceptibility (K_m) is very low (i.e. $<10^{-5}$ SI).

388

389   4.3. Palaeomagnetic results

390

391   The palaeomagnetic study was carried out on samples from Aït Labbès, Toulal and Tadaghast

392   localities. The average measured directions for specimen, sites and localities with the

393   corresponding statistical parameters are reported in **Table 2**.

394

395   *4.3.1. Aït Labbès deposit*

396

397   Stepwise demagnetization shows two principal magnetic components for red ore

398   samples distinguished at about 100-150°C (**Figures 11a and 11b**). The low-temperature

399   component (LTC) below 100-150°C is plunging downwards but its direction is scattered, not

consistent with the present-day geomagnetic field. The Characteristic Remanent Magnetization (ChRM) decays to the origin and is, either south to south-southwestwards and plunging upwards (**Figure 11a**) or north to northeastwards and plunging downwards (**Figure 11b**). Although the two opposed polarities are not strictly antipodal, and the reversal test (McFadden and McElhinny 1990) is negative (**Figure 11c**), the average direction of the two groups are similar within errors and a specimen-mean direction for red ore can be calculated at D = 11.1°, I = 42.8°, k = 31, α_{95} = 4.9°, with D and I as the respective declination and inclination of the remanent magnetization, k as the precision parameter and α_{95} as the radius of the 95% confidence circle (**Table 2**). After removing a scattered LTC, internal sediment specimens display a CHRM pointing toward to the origin (**Figure 11d**) with an unblocking temperature over 100-150°C. This component is chiefly north to north-northeastward and plunging upwards (**Figure 11d**). In addition, a south to southeastward and downward component is also observed from two specimens (**Figure 11e**). A specimen-mean direction from internal sediment can be calculated at D = 11.5°, I = 55.0°, k = 12.5, α_{95} = 19.7°, although these two groups with opposed polarities are not strictly antipodal (**Table 2**) and the reversal test is not positive.

4.3.2. Toulal prospect

At Toulal, all samples display a scattered LTC (northwestwards and dipping downwards). Red ore samples present a ChRM decaying to the origin, with unblocking temperatures at 100-150°C. This component is either northward and downward (**Figure 12a**), or south to south-southeastward and upward (**Figure 12b**). Despite a negative reversal test, the two groups of opposed polarities are antipodal, with mean directions similar within errors; a specimen-mean direction at D = 356.0°, I = 47.3°, k = 54.0, α_{95} = 7.1°, has been calculated

for the red ore samples at this locality (**Figure 12c and Table 2**). Identically, a north-northwestward and dipping downward LTC is present in the internal sediments. The ChRM (above 250°C) points to the origin, although demagnetization is not total for several hematite rich specimens. Both northward and downward (**Figure 12d**), or south to south-southwestward and upward (**Figure 12e**) directions have been observed for this component. Despite scattering of individual specimens with reverse polarities, the two groups are antipodal with positive reversal test, and we have calculated a specimen-mean direction at D = 356.7°, I = 34.9°, k = 22.4, α_{95} = 9.4° for internal sediment (**Figure 12f and Table 2**).

4.3.3. Tadaghast deposit

Conversely at Tadaghast, both red ore and internal sediment samples present a characteristic remanence magnetization (ChRM) decaying to the origin, after removing the rare and scattered LTC. For ore specimens, the direction of this ChRM is south-southeastward and plunging upwards (**Figure 13a**). Individual data are scattered (**Figure 13b**) and the calculated specimen-mean at D = 154.4°, I = -57.2°, k = 18.7, α_{95} = 18.2° displays a high statistical variability (**Table 2**). For internal sediment, the direction of ChRM is northeastward and plunging downward (**Figure 13c**). Oppositely, data are grouped and at a specimen-mean has been calculated at D = 20.3°, I = 34.1°, k = 216.1, α_{95} = 4.1° (**Figure 13d and Table 2**).

4.3.4. Beni Tajite deposit

Only 4 specimens out of 10 measured samples have produced a significant remanent magnetization, probably due to a low concentration in ferromagnetic minerals. A ChRM component has been isolated between 300°C and 600°C (**Figure 13e**). As its direction is

450 relatively scattered and the number of specimen is small (**Figure 13f**), we cannot compute an

451 average paleomagnetic direction and utilize it for dating this deposit.

452

453 **5. Discussion**

454

455 5.1. Internal structures of non-sulphide Zn-Pb deposits

456

457 Investigation of magnetic carriers has shown that internal sediment and red ore contain

458 soft coercive minerals, magnetite and minor maghemite, and hard coercive minerals, like

459 goethite with minor hematite (**Figure 7 and 8**). In grey ore and host limestone, the dominant

460 magnetic carriers of susceptibility and remanence are often diamagnetic and paramagnetic

461 minerals, although several samples may include a small amount of magnetite (**Figure 7**).

462 Iron oxi-hydroxides have been observed under optical and electronic microscopes in

463 all deposits. Choulet et al. (2014) have established that both minerals pseudomorph pyrite

464 depending on local pH conditions during early stage of supergene weathering. In addition,

465 goethite may occur later in the succession to form thin bands that alternate with drusy

466 smithsonite (**Figures 3b and 3c**) or to fill voids within geodes (**Figure 3d**). In all cases,

467 goethite and hematite precipitate from iron-saturated solution, implying that the magnetic

468 property, especially the magnetic remanence of the high temperature component partly carried

469 by hematite is of chemical origin. In internal sediments, the iron oxi-hydroxides (hematite and

470 goethite) have formed during diagenesis and thus imply a remanent magnetization of

471 chemical origin too. However, the magnetic remanence is often totally removed at 580°C, so

472 that chemical remanent magnetization is not the dominant one in both types of rocks. Our

473 study of the magnetic mineralogy has also shown the ubiquitous occurrence of magnetite. In

474 sedimentary rocks, magnetite is of detrital origin and its magnetic properties have been

475 acquired during particle deposition. Magnetite can also be formed during diagenesis and long-

476 lived burial (Aubourg et al. 2012), but such conditions (depth > 2km) have not been reached

477 in karst-related internal sediments as well as in red ore veins. Red ore is characterized by a

478 formation under an oxidizing environment, not compatible with the precipitation of

479 magnetite, especially under supergene conditions. Two hypotheses for the presence of

480 magnetite can be advanced: 1) recycling of detrital magnetite initially within the limestone,

481 but released after host rock dissolution, 2) occurrence of very small cavities of internal

482 sediments including detrital magnetite, which is frequently observed in ore samples (Choulet

483 et al. 2014). These results are partly consistent with the magnetic mineralogy investigated in

484 Sardinian non-sulphide ore deposits (Boni et al. 2005). Goethite and hematite represented the

485 main magnetic carriers and magnetite was not identified, as they did not collect samples

486 related to detrital processes, like karstic internal sediment.

487 According to AMS measurements, internal sediment samples present a sub-horizontal

488 magnetic foliation (**Figures 9 and 10**). A similar pattern is sometimes observed for ore

489 samples, although a local disturbance is also recorded. The data are more scattered in the host

490 limestone, but data are more distributed along a girdle that became horizontal after bedding

491 correction. This suggests that this pre-tilting magnetic fabric was initially horizontal and

492 could correspond to sedimentary deposition. Whatever the rock type, the magnetic lineation is

493 regularly NW-SE to W-E trending (**Figures 9 and 10**), which is consistent with the

494 orientation of the karstic cavities (**Figure 2**). AMS parameters and, especially, the corrected

495 anisotropy degree are generally low for ore and internal sediment (**Table 1**), suggesting that

496 post-deposition deformation is absent or not penetrative. The broad similarity of AMS

497 patterns between ore and internal sediment implies that same parameters control the

498 development of rock internal fabrics. As magnetic lineation parallels the trend of karst-related

499 cavities and magnetic foliation is horizontal whatever the morphology of the cavity, we

suggest that sedimentary processes within the cavity related to karst fluid dynamics driven by the regular network of first order fractures may control the internal structure of infilling material. In addition, the strong obliquity between horizontal magnetic foliation and the surrounding tectonic markers (faults, limestone bedding) argue for a post 40 Ma deposition of ores and internal sediments, after the main tectonic episode of Atlas (Frizon de Lamotte et al. 2009).

Locally, the individual specimens are scattered for a given site (e.g. AL1, AL2; **Figure 9a**), or define an oblique foliation (**Figure 10b**). This perturbation of the AMS signal may be explained by sedimentary recycling of ore and barren material during karst evolution (e.g. for Aït Labbès). In addition, the Atlas range results from multiple superimposed compressive events (Frizon de Lamotte et al. 2009), and these successive reactivations could explain the oblique fabric exemplified at Tadaghast. Hence it is highly probable that the karstic network has formed progressively throughout the Moroccan High Atlas, in relation with major compression events. Although most observations have revealed horizontal bedding in the cavity, early internal karstic sediment may have undergone polyphased tectonics and, as a consequence, the originally horizontal fabric has been tilted or removed during the recent uplift episodes.

5.2. Age(s) of Moroccan High-Atlas non-sulphide Zn-Pb deposits

At Aït Labbès and Toual localities, we obtained a well-defined ChRM and chiefly antipodal directions that allow us to calculate mean site directions (**Figures 11 and 12**). The presence of two antipodal polarities for each rock type suggests that remanence is not due to a remagnetization and that our dataset averages the secular variations of the Earth magnetic field. This is also confirmed by our investigation of the magnetic mineralogy that suggests

magnetite and hematite as respective carriers of detrital and chemical remanence, acquired

during ore and sediment deposition or during late weathering. Although the primary origin of

magnetization cannot be surely assessed, the partial detrital origin for remanence may be

underlined by general horizontal bedding observed in the field and the shallow inclination of

AMS planar fabric. Although for some samples from Aït Labbès the magnetic fabric is not

horiziontal, this does not have significant influence on the scattering of remanent directions.

At Tadaghast, we obtained a well-constrained direction for internal sediment, but the

individual measurements for red ore are very scattered (**Figure 13**). For each lithology, a sole

polarity has been measured, so that the contemporaneity of ore and internal sediment cannot

be ascertained. Given our dataset, it is clearly impossible to advocate a primary chemical or

detrital origin of the remanence and the hypothesis of late weathering cannot be ruled out. In

addition, specimen-mean directions are not consistent between the two rock types and this can

be explained by: 1) false orientation of the specimen, because cores have been drilled at lab

from an oriented hand sample and 2) magnetic reworking, as AMS fabrics of red ore (**Figure

10**) are clearly oblique suggesting post-deposition tectonics or recent weathering. Despite a

relatively good consistency between Tadaghast internal sediments and other localities, we

cannot guarantee the reliability of these data, therefore we have excluded them from further

interpretation.

As specimen-mean directions calculated for red ore and internal sediment are

compatible for each locality (**Table 2**), we computed a specimen-mean direction including

these two lithologies at D = 11.1°, I = 44.8°, k = 24.2, α_{95} = 5.0° for Aït Labbès and at D =

356.4°, I = 40.3°, k = 26.5, α_{95} = 6.3° for Toulal (**Figure 14**). Furthermore, we have

calculated two palaeomagnetic poles: λ = 114.4°N, Φ = 78.6°E, dp/dm = 4.0°/6.4° for Aït

Labbès (32.38°N, -4.33°E) and λ = 196.7°N, Φ = 79.9°E, dp/dm = 4.2°/6.9° for Toulal

(32.30°N, -3.99°E). These two poles are statistically different within error. As several

550 measured specimens display reverse polarity, the upper age limit for localities corresponds to

551 the last magnetic reversal (Brunhes-Matuyama reversal) at ca. 0.78 Ma (Gradstein et al.

552 2004). **Figure 15** provides a comparison with the Apparent Polar Wander Path (APWP) of

553 Africa (Besse and Courtillot 2002). The Toulal pole is slightly isolated from the APWP but

554 the ellipse of confidence crosscuts the APWP individual poles at 10 Ma, 20 Ma and 30 Ma.

555 Hence, an age between 30 Ma and 10 Ma can be proposed for Toulal. This is consistent with

556 the horizontal AMS fabric that suggested post-tectonics deposition of red ore and internal

557 sediments after the main Atlas episode at ca. 40 Ma (Frizon de Lamotte et al. 2009).

558 Conversely, the palaeomagnetic pole calculated for Aït Labbès intersects the APWP and the

559 age is statistically between 60 Ma and 10 Ma. However, field observation suggested that red

560 ore and internal sediment do not predate the major compression episode at 40 Ma. Hence the

561 age of Aït Labbès pole is bracketed between 40 Ma and 10 Ma, and in detail, the pole plots

562 closer to the 40 Ma pole of APWP than to the younger one's (**Figure 15**). The apparent

563 diachronism between these two localities is in accordance with the differences in AMS

564 fabrics. The AMS pattern at Toulal shows a well-defined horizontal magnetic foliation and a

565 consistent magnetic lineation whose direction parallels the trend of the karst-related cavity.

566 Conversely, both magnetic foliation and lineation are badly constrained at Aït Labbès,

567 suggesting tectonic and sedimentary perturbations after ore and internal sediment deposition.

568   Palaeomagnetic data support the post-Atlasic age of supergene weathering inferred

569 from field observation (Choulet et al. 2014), but we could not improve this time interval,

570 similarly to Boni et al. (2003) for Sardinia non-sulphide ore deposits. The large age span of

571 our data can be explained by the limited dataset, although narrow ellipses of confidence for

572 pole attest for the reliability of data. Beyond statistically and sampling bias, the limited

573 movements of Africa during the last tens of million years (Besse and Courtillot 2002)

574 preclude a better constraint for recent episodes when age is based on palaeomagnetism.

575

576 5.3. Integration into the Moroccan High-Atlas geodynamic context

577

578   This study is the first attempt of dating the non-sulphide zinc deposits in the Moroccan

579 High Atlas. The obtained results are consistent with the timing of ore deposition proposed in

580 Choulet et al. (2014). The following evolution may be proposed:

581   (1) During Mesozoic (**Figure 16a**), the opening of the Atlantic Ocean and the Tethys

582 led to the reactivation of Variscan deep structures into normal faults that control the formation

583 of a series of horsts and grabens (Laville and Piqué 1991; Piqué 1994). During the Early

584 Jurassic, the formation of carbonate platforms with reef limestone in shallow domains is

585 accompanied by deposition of Zn-Pb sulphide lenses throughout the future High Atlas domain

586 (Mouguina 2004). These deposits are mainly concordant with the bedding of the host rock

587 (Leblanc 1968). As presented in section 2, discontinuous sedimentation has been recorded

588 afterwards, until Tertiary inversion tectonics (Frizon de la Motte et al. 2009).

589   (2) Between 50 Ma and 35Ma, western Mediterranean domains experienced

590 shortening due to convergence between Europe and Africa (**Figure 16b**). As a consequence,

591 the area has recorded compressive tectonics, leading to the formation of the High Atlas fold-

592 and-thrust belt (Frizon de la Motte et al. 2000; 2009). Reactivation of Liassic normal faults

593 into thrusts has controlled the localisation of narrow anticlines (Teixell et al. 2003), as

594 exemplified at Aït Labbès and Toulal (**Figure 16c**). This compression is not responsible for

595 the present topography but can account for a regional uplift, intense erosion and subsequent

596 exhumation of Zn-Pb sulphide lenses. When the water table has fallen down, dissolution of

597 host limestone may have started, as well as supergene oxidation of the sulphide protore

598 (Choulet et al. 2014). The upright position of the ore lenses has facilitated the downward

599 percolation of the surface water leading to the formation of non-sulphide Zn ore deposits.

24

600   Coevally, infilling of karst-related cavities has occurred, either as internal karstic

601   sedimentation or as a precipitation from a Zn-rich solution. Both rock types acquired their

602   fabrics, marked by horizontal foliation and lineation tending to be parallel to the trend of

603   dissolution cavities, controlled by the hydrodynamic regime within the karst. Despite a

604   regional arid climate and relatively quiet tectonics between 35Ma and 5Ma (Maley 1980),

605   short wet episodes (Le Houérou 1997) have contributed to enlargement of karst network and

606   deepening of supergene weathering front.

607   (3) Since 3Ma, a second major shortening episode has affected northern Africa

608   (**Figure 16d**; Frizon de Lamotte et al. 2000; 2009). Although this episode is widely observed

609   and responsible for the present topography (**Figure 16e**), it seems that its effects on non-

610   sulphide Zn ore deposits of Moroccan High-Atlas has remained limited, as magnetic foliation

611   and sedimentary bedding are mostly preserved as horizontal. Conversely, at Aït Labbès or at

612   Tadaghast, the absence of a well-defined foliation or the oblique pattern of the fabric may

613   indicate that this second compression episode has modified the AMS and remanent

614   magnetisation primary patterns. The widespread reverse polarities constrain the upper limit

615   for oxidation to 0.78 Ma and the last reversal of the Earth magnetic field.

616

617   **6. Conclusions**

618

619   This is the first attempt of AMS study within non-sulphide Zn ore deposits. It provides

620   crucial information on internal fabrics within ores and on the first-order geometric

621   connections between ore and internal karstic sediment. Results are consistent with field

622   observation and previous interpretations (Choulet et al. 2014). Hence, the dominantly

623   horizontal magnetic foliation and the direction of magnetic lineation that tends to be parallel

624   to the karstic cavities alignment may attest for a control of fabrics by karst hydrodynamics.

Locally, rock magnetism signal has been removed or fabrics have been tilted due to late superimposed tectonic events.

Palaeomagnetism was successfully applied on both ore and internal karstic sediment from three deposits and obtained results are compatible with age constraints inferred from field observations. Our results support a post-tilting paleomagnetic record that we interpret as of primary origin; it has been acquired either during chemical alteration of ore vein due to rock exhumation or during internal sedimentation processes resulting in the filling of karst-related cavities. Results also suggest local diachronism between deposits, probably due to differences of uplift across the range. However, this last conclusion may be tempered, as our age resolution is not statistically acceptable and we are not able to narrow the time interval between Late Eocene and the last magnetic reversal. The restricted sampling and the limited absolute movement of Africa during the last tens millions years may explain this issue.

As inferred by Boni et al. (2005), this study has shown that palaeomagnetism can be used to constrain the timing of supergene oxidation and the formation of non-sulphide ore deposits. In addition, coupling specimens collected from internal karstic sediment and ore may provide robust results, especially when the rock fabric is controlled by AMS parameters and patterns. Although Sardinian and Moroccan deposits are not ideal cases for high resolution dating, this method may be applied on other examples throughout the world (Belgium, Iran, Vietnam…). In the case of historic deposits of Belgium (Dejonghe 1998), this method could be of great benefit, as field observation only provides a timing of formation between Visean and Cretaceous (Coppola et al. 2008). Besides, the occurrence of supergene willemite mineralisation and its possible use for geochronology (Schneider et al. 2008) may represent a good opportunity to compare both methods and assess the utilisation of palaeomagnetism to timely constrain oxidation episodes.

7. Acknowledgements

8. References

Agard J, du Dresnay R (1965) La région minéralisée du Jbel Bou-Dahar, près de Beni Tajjit (Haut-Atlas oriental) : Étude géologique et métallogénique. Notes et Mém Serv Géol Maroc 181:135-166 (in French).

Auajjar J, Boulègue J (1999) Les minéralisations Pb-Zn-(Cu) Ba du socle paléozoïque et de la plate-forme liasique du district du Tazekka (Taza, Maroc oriental): une synthèse. Chron Rech Min 536-537:121-135 (in French).

Aubourg C, Pozzi J-P, Kars M (2012) Burial, claystones remagnetization and some consequences for magnetostratigraphy. Geol Soc London, Sp Pub 371:181-188.

Bazin D (1968) Etude géologique et métallogénique des chaînons atlasique du Tizi n'Firest au Nord de Ksar-es-Souk, Maroc. Notes et Mém Serv Géol Maroc 206:37-114 (in French).

27

673

674   Besse J, Courtillot V (2002) Apparent and true polar wander and the geometry of the

675   geomagnetic field over the last 200 Myr. J Geophys Res 107:doi:10.1029/2000JB000050.

676

677   Boni M, Gilg HA, Aversa G, Balassone G (2003) The "Calamine" of SW Sardinia (Italy):

678   geology, mineralogy and stable isotope geochemistry of a supergene Zn mineralization. Econ

679   Geol 98:731-748.

680

681   Boni M, Dinarès-Turell J, Sagnotti L (2005) Paleomagnetic dating of non-sulfide Zn-Pb ores

682   in SW Sardinia (Italy): a first attempt. Ann of Geoph 48:301-312.

683

684   Boni M, Terracciano R, Evans N, Laukamp C, Schneider J, Bechstädt T (2007) Genesis of

685   vanadium ores in the Otavi Mountainland (Namibia). Econ Geol 102:441-469.

686

687   Boni M, Balassone G, Arseneau V, Schmidt P (2009) The non-sulphide zinc deposit at Accha

688   (Southern Peru): geological and mineralogical characterization. Econ Geol 104:267-289.

689

690   Borg G (2003) Surface-related formation, upgrading, and improvement of ore deposits - a

691   review of supergene metallogenic processes. In: Eliopoulos DG et al. (Ed.), Mineral

692   Exploration and Sustainable Development. Millress, 61-64.

693

694 Borg G, Kärner K, Buxton M, Armstrong R, van der Merve, Schalk W (2003) Geology of the

695 Skorpion non-sulphide deposit, southern Namibia. Econ Geol 98:749-771.

696

697 Borg G (2009) The role of fault structures and deep oxidation in supergene base metal

698 deposits. In: Titley SR (Ed.), Supergene Environments, Processes and Products. Econ Geol

699 Spec Publ 14:121-132.

700

701 Bouchaou L (1988) Hydrogéologie du basin des sources karstiques du complexe calcaire

702 Haut-Atlasien du Dir de Beni-Mellal (Maroc). Dissertation, Université de Besançon (in

703 French).

704

705 Bradley DC, Leach DL (2003) Tectonic controls of Mississippi Valley-type lead-zinc

706 mineralization in orogenic forelands. Miner Deposita 38:652-667.

707

708 Brechbühler YA, Bernasconi R, Schaer JP (1988) Jurassic sediments of the Central High

709 Atlas of Morocco: deposition, burial and erosion history. In: Jacobshagen V (Ed.), The Atlas

710 System of Morocco. Lect Notes Earth Sci 15:139-168.

711

712 Bruyère D, De Putter T, Decrée S, Dupuis C, Fuchs Y, Jamoussi F et al (2010) Miocene

713 karsts and associated Fe-Zn-rich minerals in Aïn Khamouda (Central Tunisia). J Afr Earth Sci

714 57:70-78.

715

716 Caïa J (1968) Roches éruptives basiques et minéralisations en plomb, zinc et strontium de la

717 région de Tirrhist (Haute-Atlas de Midelt). Notes et Mém Serv Géol Maroc 206:7-30 (in

718 French).

719

720 Charles N, Faure M, Chen Y (2009) The mechanism emplacement of the Montagne Noire

721 migmatitic dome (French Massif Central): New insights from petrofabric and AMS studies. J

722 Struct Geol 31:1423-1440.

723

724 Charles N, Gumiaux C, Augier R, Chen Y, Faure M, Lin W, Zhu R (2012) Metamorphic Core

725 Complex dynamics and structural development: Field evidences from the Liaodong Peninsula

726 (East China). Tectonophysics 560-561:22-50.

727

728 Charrière A, Haddoumi H, Mojon PO (2005) Découverte de Jurassique supérieur et d'un

729 niveau marin du Barrémien dans les "couches rouges" continentales du Haut-Atlas central

730 marocain : implications paléogéographiques et structurales. C R Palevol 4:385-394 (in

731 French).

732

733 Charrière A, Haddoumi H, Mojon PO, Ferrière J, Cuche D, Zili L (2009) Mise en évidence

734 par charophytes et ostracodes de l'âge paléocène des dépôts discordants sur les rides

735 anticlinales de la région d'Imilchil (Haut-Atlas, Maroc): conséquences paléogéographiques et

736 structurales. C R Palevol 8:9-19 (in French).

737

738 Chèvremont P (1975) Les roches éruptives basiques des boutonnières de Tassent et Tasraft et

739 leurs indices métallifères dans leur cadre géologique (Haut-Atlas central, Maroc).

740 Dissertation, Université Claude-Bernard, Lyon (in French).

741

742 Choulet F, Charles N, Barbanson L, Branquet Y, Sizaret S, Ennaciri A, Badra L, Chen Y

743 (2014) Non-sulfide zinc deposits of the Moroccan High Atlas: Multi-scale characterization

744 and origin. Ore Geol Rev 56:115-140.

745

746 Cogné JP (2003) PaleoMac: a Macintosh™ application for treating paleomagnetic data and

747 making plate reconstructions. Geochem Geophys Geosyst

748 4(1):1007.doi:10.1029/2001GC000227.

749

750 Cole PM, Sole KC (2002) Solvent extraction in the primary and secondary processing of

751 zinc. J South Afr Inst Min Metall 102:451-456.

752

753 Coppola V, Boni M, Gilg HA, Balassone G, Dejonghe L (2008) The "calamine" nonsulfides

754 Zn-Pb deposits of Belgium: petrographical, mineralogical and geochemical characterization.

755 Ore Geol Rev 33:187-210.

756

757   Couvreur G (1978) Le rôle de la lithologie dans l'évolution des formes karstiques majeures du

758   Haut Atlas central calcaire (Maroc). Rev Geogr Phys 66:309-311 (in French).

759

760   Daliran F, Borg G, Armstrong R, Walther J, Vennemann T, Friese K et al (2009) Non

761   sulphide zinc deposits, Iran - the hypogene emplacement and supergene modification history

762   of the Angouran Zinc Deposit, NW-Iran. Berichte zur Lagerstätten und Rohstoffforschung,

763   57. Bundesanstalt für Geowissenschaften und Rohstoffe, Hannover, 75 p.

764

765   Daliran F, Pride K, Walther J, Berner ZA, Bakker RJ (2013) The Angouran Zn-(Pb) deposit,

766   NW Iran: Evidence for a two stage, hypogene zinc sulphide-zinc carbonate mineralization.

767   Ore Geol Rev 53:373-402.

768

769   Decrée S, Marignac C, De Putter T, Deloule E, Liégeois JP, Demaiffe D (2008) Pb-Zn

770   mineralizations in a Miocene regional extensional context: the case of the Sidi Driss and the

771   Douahria ore deposits (Nefza mining district, N. Tunisia). Ore Geol Rev 34:285-303.

772

773   Decrée S, Ruffet G, De Putter T, Baele JM, Recourt P, Jamoussi et al (2010) Mn oxides as

774   efficient traps for metal pollutants in a polyphase low-temperature Pliocene environment: a

775   case study in the Tamra iron mine, Nefza mining district, Tunisia. J Afr Earth Sci 57:249-261.

776

777   Dejonghe L (1998) Zinc-lead deposits of Belgium. Ore Geol Rev 12:329-354.

778

779   du Dresnay R (1979) Sédiments jurassiques du domaine des chaînes atlasiques du Maroc.

780   Symposium "Sédimentation jurassique ouest-européenne", ASF Publ Spéc 345-365 (in

781   French).

782

783   du Dresnay R (1988) Recent data on the geology of the Middle Atlas (Morocco). In:

784   Jacobshagen V (Ed.), The Atlas System of Morocco. Lect Notes Earth Sci 15:293-320.

785

786   Emberger A (1965) Carte polygénétique des minéralisations plombifères de la Haute

787   Moulouya (gisements d'Aouli, Mibladen et Zaida), Maroc. C R Acad Sci Paris 260:3433-3436

788   (in French).

789

790   Emberger A (1969) Carte des minéralisations plombo-zincifères du Maroc : gîtes et indices

791   renfermant du plomb ou du zinc en élément majeur ou mineur. Notes et Mém Serv Géol

792   Maroc 215 (in French).

793

794   Essalhi M, Sizaret S, Barbanson L, Chen Y, Branquet Y, Panis D, Camps P, Rochette P,

795   Canals A (2009) Track of fluid paleocirculation in dolomite host rock at regional scale by the

796   Anisotropy of Magnetic Susceptibility (AMS): An example from Aptian carbonates of La

797   Florida, Northern Spain. Earth Planet Sci Lett 277:501-513.

798

799 Essalhi M, Sizaret S, Barbanson L, Chen Y, Lagroix F, Demory F, Nieto JM, Sáez R, Capitán

800 A (2011) A case study of the internal structures of gossans and weathering processes in the

801 Iberian Pyrite Belt using magnetic fabrics and paleomagnetic dating. Mineral Deposita.

802 doi.10.1007/s00126-011-0361-8.

803

804 Fisher RA (1953) Dispersion of a sphere. Proc Roy Soc Lond A217, 295-305.

805

806 Frizon de Lamotte D, Zizi M, Missenard Y, Hafid M, El Azzouzi M, Charrière A et al (2008)

807 The Atlas system. In: Michard A, Saddiqi O, Chalouan A, Frizon de Lamotte D (Eds.),

808 Continental Evolution: The Geology of Morocco. Structure, Stratigraphy, and Tectonics of

809 the Africa-Atlantic-Mediterranean Triple Junction. Springer-Verlag 133-202.

810

811 Frizon de Lamotte D, Leturmy P, Missenard Y, Khomsi S, Ruiz G, Saddiqi O et al (2009)

812 Mesozoic and Cenozoic vertical movements in the Atlas system (Algeria, Morocco, Tunisia):

813 an overview. Tectonophysics 475:9-28.

814

815 Gnoinski J (2007) Skorpion zinc: optimization and innovation. J South Afr Instrum Min

816 Metall 107:657-662.

817

818 Gomez F, Allmendinger R, Barazangi M, Beauchamp W (2000) Role of the Atlas Mountains

819 (northwest Africa) within the African-Eurasian plate-boundary zone. Geology 28:775-778.

820

821   Gradstein F, Ogg J, Smith A (2004) A geological time scale. Cambridge University Press, 600

822   p.

823

824   Groves I, Carman CE, Dunlap WJ (2003) Geology of the Beltana willemite deposit, Flinders

825   Ranges, South Australia. Econ Geol 98:797-818.

826

827   Haddoumi H, Charrière A, Andreu B, Mojon PO (2008) Les dépôts continentaux du

828   Jurassique moyen au Crétacé inférieur dans le Haut-Atlas oriental (Maroc) :

829   Paléoenvironnements successifs et signification paléogéographique. Carnets de Géologie -

830   Notebooks on Geology, Brest. (2008/XX (CG2008 AXX).

831   http://paleopolis.rediris.es/cg/French).

832

833   Herbig HG, Trappe J (1994) Stratigraphy of the Subatlas Group (Maastrichtian-Middle

834   Eocene, Morocco). Newsl Stratigr 30:125-165.

835

836   Heyl AV, Bozion CN (1962) Oxidized zinc deposits of the United States, part 1. General

837   geology. US Geol Surv Bull 1135-A, 52 p.

838

839   Hitzman MW, Reynolds NA, Sangster DF, Allen CR, Carman CE (2003) Classification,

840   genesis, and exploration guides for non sulfide zinc deposits. Econ Geol 98:685-714.

841

842   Hosseini SH (2008) Physicochemical Studies of Oxide Zinc Mineral Flotation. Dissertation,

843   University of Technology, Luleå.

844

845   Hrouda F (1982) Magnetic anisotropy of rocks and its application in geology and geophysics.

846   Geophys Surv 5:37-82.

847

848   Jelinek V (1981) Characterization of the magnetic fabric of rocks. Tectonophysics 79:63-67.

849

850   Jemmali N, Souissi F, Vennemann TWM, Carranza EJ (2011) Genesis of the Jurassic

851   carbonate-hosted Pb-Zn deposits of Jebel Ressas (North-Eastern Tunisia): Evidence from

852   mineralogy, petrography and trace metal contents and isotope (O, C, S, Pb) geochemistry. Res

853   Geol 61:367-383.

854

855   Kirschvink J (1980) The least squares line and the analysis of palaeomagnetic data. Geophys J

856   R Astron Soc 62:699-718.

857

858   Large D (2001) The geology of non-sulphide zinc deposits - an overview. Erzmetall 54:264-

859   276.

860

861 Laville E, Piqué A (1991) La distension crustale atlantique et atlasique au Maroc au début du

862 Mésozoïque: le rejeu des structures hercyniennes. Bull Soc Géol Fr 162:1161-1171.

863

864 Laville E, Piqué A (1992) Jurassic penetrative deformation and Cenozoic uplift in the central

865 High Atlas (Morocco): a tectonic model. Structural and orogenic inversions. Geol Rundsch

866 81:157-170.

867

868 Laville E, Piqué A, Amrhar M, Charroud M (2004) A restatement of the Mesozoic Atlasic

869 rifting (Morocco). J Afr Earth Sci 38:145-153.

870

871 Leach DL, Bradley D, Lewchuk MT, Symons DTA., de Marsily G, Brannon J (2001)

872 Mississipi Valley-type lead-zinc deposits through geological time: Implications from recent

873 age dating research. Mineral Deposita 36:711-740.

874

875 Leblanc M (1968) Etude géologique et métallogénique du Jbel Bou Arhous et de son

876 prolongement oriental (Haut-Atlas marocain oriental). Notes Mém Serv Géol Maroc 206:117-

877 206 (in French).

878

879 Le Houérou HN (1997) Climate, flora and fauna changes in the Sahara over the past 500

880 million years. J Arid Env 37:619-647.

881

882 Maley J (1980) Les changements climatiques de la fin du Tertiaire en Afrique: leurs

883 conséquences sur l'apparition du Sahara et de sa végétation. In: Williams AJ, Faure H (Eds),

884 The Sahara and the Nile. Balkema, Rotterdam, 63-86.

885

886 Mattauer M, Tapponnier P, Proust F (1977) Sur les mécanismes de formation des chaînes

887 intracontinentales. L'exemple des chaînes atlasiques du Maroc. Bull Soc Géol Fr 19:521-526.

888

889 McFadden PL McElhinny MW (1990) Classification of the reversal test in palaeomagnetism.

890 Geophys J Int 103: 725-729.

891

892 Mouguina EM (2004) Les minéralisations polymétalliques (Zn-Pb, Cu, Co, Ni) du Jurassique

893 du Haut Atlas central (Maroc): Contexte géodynamique, typologies et modèles génétiques.

894 Dissertation, Faculté des Sciences Semlalia, Marrakech.

895

896 Nicod J (1997) Karsts et fonctionnement hydrologique dans le Haut Atlas central calcaire et

897 sur la bordure du Moyen Atlas méridional. Ann Geogr 106 :536-538 (in French).

898

899 Ovtracht A (1978) Province plombo-zincifère du Haut Atlas central. Mines Géol Energie

900 44:103-109.

901

902 Pannalal SJ, Symons DTA, Sangster DF (2008) Paleomagnetic Evidence for an Early Permian

903 Age of the Lisheen Zn-Pb Deposit, Ireland. Econ Geol 103:1641-1655.

904

905 Piqué A, Michard A (1989) Moroccan Hercynides: a synopsis. The Paleozoic sedimentary

906 and tectonic evolution at the northern margin of West Africa. Am J Sci 289:286-330.

907

908 Piqué A (1994) Géologie du Maroc, les domaines régionaux et leur évolution structurale.

909 Pumag, Marrakech.

910

911 Popov A (1968) Les types morphologiques et la répartition des gisements de zinc et de plomb

912 en Algérie. Ann Min Géol 23:103-203.

913

914 Reichert J, Borg G (2008) Numerical simulation and a geochemical model of supergene

915 carbonate-hosted non-sulphide zinc deposits. Ore Geol Rev 33:134-151.

916

917 Ricordel C (2007) Datations par paléomagnétisme des paléoaltérations du Massif central et de

918 ses bordures: Implications géodynamiques. Dissertation, Ecole des Mines de Paris.

919

920 Ricordel-Prognon C, Lagroix F, Moreau MG, Thiry M (2010) Lateritic paleoweathering

921 profiles in French Massif Central: Paleomagnetic datings. J Geophys Res 115,

922 doi:10.1029/2010JB007419.

923

924 Rochette P, Jackson M, Aubourg C (1992) Rock magnetism and the interpretation of the

925 anisotropy of magnetic susceptibility. Rev Geophys 30:209-226.

926

927 Rouvier H, Perthuisot V, Mansouri A (1985) Pb-Zn deposits and salt-bearing diapirs in

928 Southern Europe and North Africa. Econ Geol 80:666-687.

929

930 Santoro L, Boni M, Herrington R, Clegg A (2013) The Hakkari nonsulfide Zn–Pb deposit in

931 the context of other non sulfide Zn-Pb deposits in the Tethyan Metallogenetic Belt of Turkey.

932 Ore Geol Rev. doi.org/10.1016/j.oregeorev.2013.01.011.

933

934 Schneider J, Boni M, Laukamp C, Bechstädt T, Petzel V (2008) Willemite (Zn_2SiO_4) as a

935 possible Rb-Sr geochronometer for dating nonsulfide Zn-Pb mineralization: Examples from

936 the Otavi Mountainland (Namibia). Ore Geol Rev 33:152-167.

937

938 Sizaret S, Chen Y, Chauvet A, Marcoux E, Touray JC (2003) Magnetic fabrics and fluid flow

939 directions in hydrothermal systems. A case study in the Chaillac Ba-F-Fe deposit (France).

940 Earth Plan Sci Lett 206:555-570.

941

942 Symons DTA, Sangster DF, Leach DL (1996) Paleomagnetic dating of Mississippi Valley-

943 type Pb-Zn-Ba deposits. Soc Econ Geol Spec Vol 4:515-526.

944

945 Symons DTA, Stratakos KK (2000) Palaeomagnetic dating of dolomitization and Mississippi

946 Valley-type zinc mineralization in the Mascot-Jefferson city district of Eastern Tennessee: a

947 preliminary analysis. In: Pueyo JJ, Cardellach E, Bitzer K, Taberner C (Ed), Geofluids III, 3rd

948 International Conference on Fluid Evolution, Migration and Interaction in Sedimentary

949 Basins and Orogenic Belts. J Geochem Explor 69-70:373-376.

950

951 Symons DTA, Smethurst MT, Ashton JH (2002). Paleomagnetism of the Navan Zn-Pb

952 Deposit, Ireland. Econ Geol 97:997-1012.

953

954 Tarling DH, Hrouda F (1993) The magnetic anisotropy of rocks. Chapman and Hall, London.

955

956 Terracciano R (2008) Willemite mineralization in Namibia and Zambia. Dissertation,

957 University of Napoli.

958

959 Théveniaut H, Freyssinet P (1999) Paleomagnetism applied to lateritic profiles to assess

960 saprolite and duricrust formation processes: The example of the Mont Baduel profile (French

961 Guiana). Palaeogeogr Palaeoclimatol Palaeoecol 148:209-231.

962

963   Théveniaut H, Freyssinet P (2002) Timing of lateritization on the Guiana Shield: Synthesis of

964   paleomagnetic results from French Guiana and Suriname. Palaeogeogr Palaeoclimatol

965   Palaeoecol 178:91-117.

966

967   Théveniaut H, Quesnel F, Wyns R, Hugues G (2007) Paleomagnetism dating of the "Borne de

968   Fer" ferricrete (NE France): Lower Cretaceous continental weathering. Palaeogeogr

969   Palaeoclimatol Palaeoecol 253:271-279.

970

971   Van der Voo R (1993) Paleomagnetism of the Atlantic, Tethys and Iapetus Oceans.

972   Cambridge University Press, New York, 411 p.

973

974   Withney DL, Evans B (2010) Abbreviations for names of rock-forming minerals. Am Miner

975   95:185-187.

976

977   Zijderveld JDA (1967) A.C. demagnetization of rocks: Analysis of results. Methods in

978   Paleomagnetism Conference, Amsterdam, Proceedings 254-286.

Figure captions

Figure 1: (a) Simplified tectonic map of western Mediterranean Sea and western North Africa, illustrating the relationships between High Atlas and the Alpine Belt (modified from Gomez et al. 2000). MA: Middle Atlas. (b) Geological map of the Moroccan High Atlas. The location of the Pb-Zn prospects (white circle) and studied ore deposits (yellow star) is also indicated. (c) Cross-section of the Moroccan High Atlas, illustrating the structure of the fold-and-thrust belt and the connection between the Mesozoic cover and the Palaeozoic basement (modified after Teixell et al. 2003).

Figure 2: (a) Panoramic view showing the typical fold-and-thrust structure of the Moroccan High-Atlas with tight and faulted anticline (Aït Labbès ore deposit). (b) View of a karstic cavity, parallel to the N80°E anticline structure, and filled by red calamine during ore extraction (Aït Labbès ore deposit). (c) Aspect of the calamine network, forming N70°E-striking boudin-like veins (Toulal prospect). (d) View of the cavities, previously filled by red ore (Toulal prospect). (e) View of a profile showing stratabound mineralisation, with distribution of Zn-Pb sulphides minerals (bottom) and Zn-Pb non-sulphides minerals (top) (Tadaghast ore deposit). (f) Relation between tilted limestone strata and horizontal marl of internal sediments filling a karstic cavity whose limit is indicated by red dashed line (Toulal prospect). (g) Sample of Zn sulphides and non-sulphides minerals (sphalerite ZnS, smithsonite $ZnCO_3$, Fe-oxides, and hemimorphite $Zn_4Si_2O_7(OH)_2 \cdot (H_2O)$) from Toulal. (h) Red ore sample made of smithsonite and Fe-oxides from Aït Labbès ore deposit. (i) Grey ore sample made of smithsonite, hemimorphite and hydrozincite ($Zn_5(CO_3)_2(OH)_6$) from Beni Tajite ore deposit. Abbreviations for minerals according to Whitney and Evans (2010): Gn: galena, Hmp: hemimorphite, Hyd: hydrozincite, Sp: sphalerite.

1004

1005   **Figure 3**: Microphotographs of non-sulphide Zn-Pb ores (a to d) and karst internal sediments

1006   (e and f) from studied ore deposits. (a) Relics of sphalerite and pyrite (protore) associated

1007   with translucent smithsonite. (TL, nic. //). (b) Iron oxi-hydroxides (goethite and hematite)

1008   encrusting oxidized smithsonite, both constituting the "red calamine" (RL, nic. //). (c)

1009   Alteration stage II smithsonite ("grey ore") growing on primary oxidized stage I smithsonite

1010   and postdating the formation of iron oxi-hydroxides. The final filling is made of

1011   hemimorphite and calcite (RL, nic. +). (d) "Grey ore" with alteration stage II smithsonite

1012   encrusting alteration stage I smithsonite and iron oxides (TL, nic. //). Zoom box: concentric

1013   shells of goethite rhythmically encrusting translucent smithsonite (TL, nic. +). (e) Internal

1014   sediments: banded Fe-oxides (hematite and goethite) encrusting banded calcite. Others micro-

1015   beds are made of smithsonite and Fe-oxides clasts. Note the presence of a smithsonite clast.

1016   (TL, nic. +). (f) Zoom on a clastic micro-bed within internal sediments. Clasts of Fe-oxides

1017   are cemented by calcite (TL, nic. //). (g) Synoptic paragenetic sequence of observed minerals

1018   in studied ore deposits. Vertical lines represent the separation between the protore

1019   mineralisation (sulphides) and the two supergene stages (i.e. red-ore and grey-ore). Vertical

1020   dashed line corresponds to the limit between the "red ore" and the "grey ore" (modified after

1021   Choulet et al. 2014). Mineral abbreviations according to Whitney and Evans (2010): Cal:

1022   calcite, Gth: goethite, Hem: hematite, Hmp: hemimorphite, Py: pyrite, Qz: quartz, Sm:

1023   smithsonite, Sp: sphalerite. RL: reflected light, TL: transmitted light, nic. //: plane polarized

1024   light, nic. +: crossed polarized light.

1025

1026   **Figure 4**: AMS and palaeomagnetic sampling sites. (a to d) Aït Labbès ore deposit sampling

1027   sites. In the sampled zone, the dip of the limestone is about 20° to the NW. (e and f) Toual

1028   prospect sampling sites. (g) Beni Tajite ore deposit with localisation of sampling sites within

1029   galleries. (h and i) Tadaghast ore deposit sampling sites into mineralised E-W vein (h) and

1030   horizon (i).

1031

1032   **Figure 5**: X-ray diffraction patterns of rock powders from Aït Labbès (a), Toulal (b), Beni

1033   Tajite (c) and Tadaghast (d) ore deposits. Intensities (y axis) are normalised to the value of the

1034   highest peak.

1035

1036   **Figure 6**: Histogram of bulk magnetic susceptibility (K_m) of all measured samples.

1037

1038   **Figure 7**: Results of Isothermal Remanent Magnetization (IRM) measurements.

1039

1040   **Figure 8**: Results of magnetic remanence measurements (a to c and e to g) and

1041   thermomagnetic Curie temperature analyses (d and h) for samples of red calamine and

1042   internal sediments from Aït Labbès, Toulal and Tadaghast. Abbreviations: HC: heating

1043   component, CC: cooling component.

1044

1045   **Figure 9**: AMS results from Aït Labbès deposit (a) and Toulal prospect (b) for non-sulphide

1046   Zn ore, internal sediments and host-rock. Results are represented by equal-area projection of

1047   each site. Squares, triangles and circles stand for K_1 (magnetic lineation), K_2 (intermediate

1048   axis) and K_3 (pole of magnetic foliation), respectively. Small grey dots and larger black ones

1049   represent individual specimen and site-mean direction, respectively. Confidence ellipses at

1050   95% level are drawn for each site-mean direction. AMS scalar parameters are represented by

1051   graphs: T (shape parameter) *vs.* P_J (corrected anisotropy parameter), T *vs.* K_m (mean bulk

1052   magnetic susceptibility) and P_J *vs.* K_m. Calculations of T and P_J can be found in Jelinek

1053   (1981). Red line indicates the karst cavity azimuth (~N50° for Aït Labbès and ~N80° for

1054   Toulal).

1055

1056   **Figure 10**: AMS results for Beni Tajite deposit (a) and Tadaghast deposit (b). See Figure 9

1057   for details.

1058

1059   **Figure 11**: Palaeomagnetic results for the Aït Labbès deposit. Orthogonal projections of

1060   sample demagnetization (Zijderveld 1967) show reverse (a) or normal (b) polarity for red ore

1061   (a) and reverse or normal (d) polarity for internal sediments. Equal-area projections show red

1062   ore (c) and internal sediments (e) specimen directions (grey dots) with locality-mean direction

1063   (black star), isolated from high temperature or high coercive AF components. Black diamond

1064   indicates the position of present-day earth magnetic field.

1065

1066   **Figure 12**: Palaeomagnetic results for the Toulal prospect. Orthogonal projections of sample

1067   demagnetization (Zijderveld 1967) show normal (a) or reverse (b) polarity for red ore and

1068   normal (d) and reverse (e) polarity for internal sediments. Equal-area projections show red ore

1069   (c) and internal sediments (f) specimen directions (grey dots) with locality-mean direction

1070   (black star), isolated from high temperature or high coercive AF components. Black diamond

1071   indicates the position of present-day earth magnetic field.

1072

1073   **Figure 13**: Palaeomagnetic results for the Tadaghast deposit (a to d) and Beni Tajite (e and f).

1074   Orthogonal projections of sample demagnetization (Zijderveld 1967) showing reverse polarity

1075   for red ore (a) and normal polarity for internal sediments (c). Equal-area projections show red

1076   ore (b) and internal sediments (d) specimen directions (grey dots) with locality-mean direction

1077   (black star), isolated from high temperature or high coercive AF components. Orthogonal

Figure 14: Equal-area projection of specimen remanence directions for both red ore (circles) and internal sediment (triangles) for Aït Labbès (a) and Toulal (b). Stars represent the locality-mean direction.

Figure 15: Palaeomagnetic poles calculated for Aït Labbès and Toulal compared to the APWP of Africa between 100 and 10 Ma (Besse and Courtillot 2002). It appears Aït Labbès and Toulal ore deposits are diachronic.

Figure 16: Tectonic sketches illustrating the development of the non-sulphide Zn-Pb deposits during the evolution of the Moroccan High Atlas with the western Mediterranean area (modified from Choulet et al. 2014, Jolivet et al. 2000; Frizon de Lamotte et al. 2000; 2009). (a) The opening of Atlantic Ocean and Tethys is accommodated by normal faulting. This period corresponds to deposition of reef and para-reef limestones and formation of sulphide lenses. (b and c) During Eocene, normal faults were reactivated as thrusts that accommodate the formation of tight anticlines, related to the High-Atlas intra-continental belt. (d and e) Atlasic main folding stage has involved a verticalization of the stratabound lenses of sulphides and has been followed by successive uplift periods, until Present, which have facilitated the percolation of meteoritic water, the karst formation (deposition of internal sediment) and the coeval to subsequent replacement of sulphide ores by non-sulphides ores.

1102 **Table 1**: AMS results from red and white ores, internal sediments and host limestone. n: number of specimen taken into statistic calculation; N: number of measured specimen. D, I, α_{95min}, α_{95max} are declination, inclination, Jelinek's statistic confidence at 95% level (Jelinek 1981) in degrees, respectively. P_J: Corrected anisotropy degree, T: Anisotropy shape parameter (Jelinek 1981), and K_m: Mean magnetic susceptibility.

1107

1108 **Table 2**: Palaeomagnetic results from red ore and internal sediments samples collected in the Moroccan High Atlas. n is the number of steps used in Kirschvink's principal component analysis (PCA), N is the number of specimens used for calculation specimen-mean direction, D and I are the respective declination and inclination of the remanent magnetization, MAD is the main angle deviation obtained from PCA, k is the precision parameter and α_{95} is the radius of the 95% confidence circle.
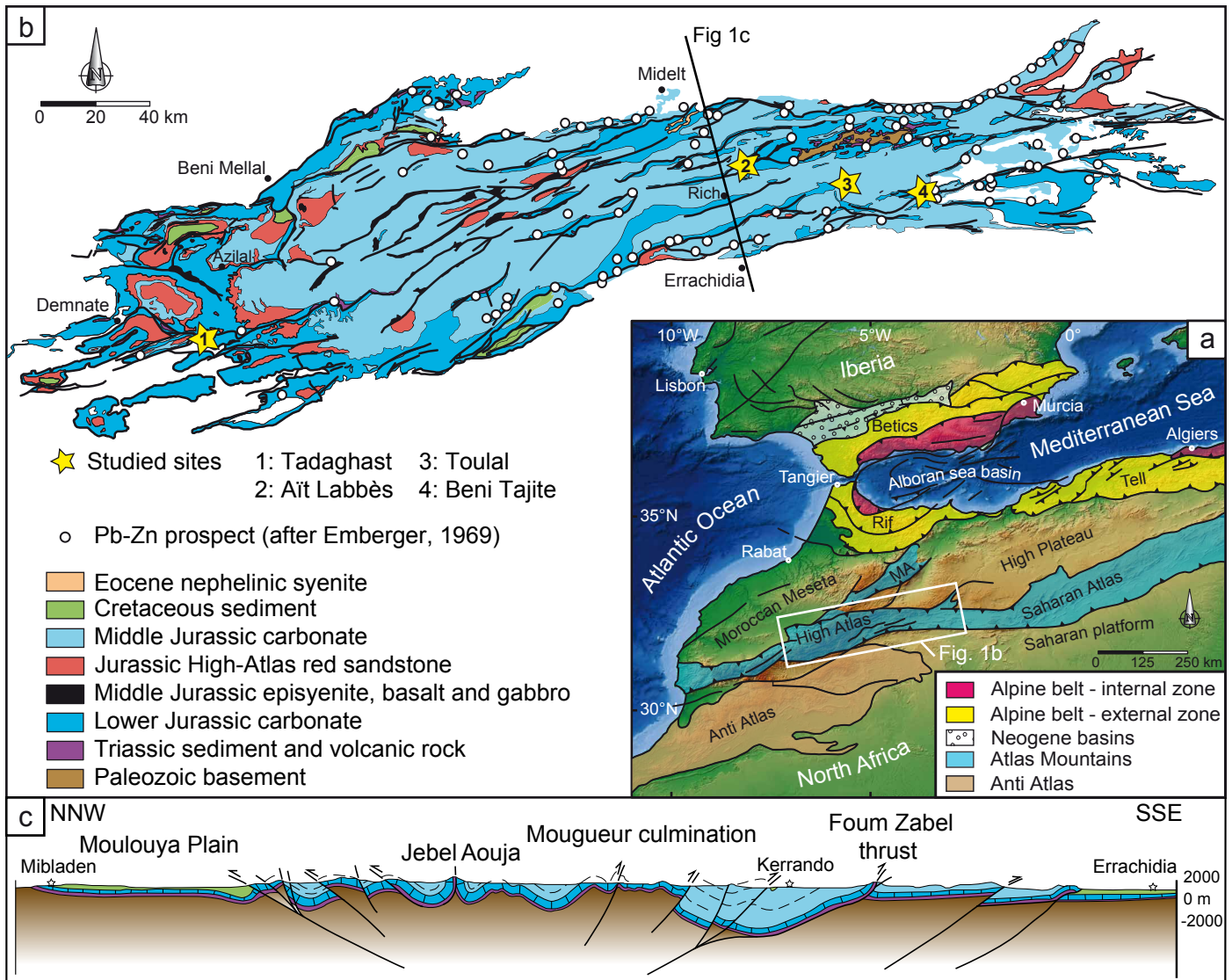
Figure 1

b

Studied sites
- 1: Tadaghast
- 2: Aït Labbès
- 3: Toulal
- 4: Beni Tajite

o Pb-Zn prospect (after Emberger, 1969)

- Eocene nephelinic syenite
- Cretaceous sediment
- Middle Jurassic carbonate
- Jurassic High-Atlas red sandstone
- Middle Jurassic episyenite, basalt and gabbro
- Lower Jurassic carbonate
- Triassic sediment and volcanic rock
- Paleozoic basement

a

Alpine belt - internal zone
Alpine belt - external zone
Neogene basins
Atlas Mountains
Anti Atlas

c NNW — SSE

Figure 1

Figure 2

a *N260* — Faulted anticline — fault — N260

b *N260*

c N70 — 20 cm

d N80

e Red ore (Sm-Fe oxides) — White ore (Hyd-Hmp) — Massive sulphides (Sp-Gn)

f bedding (host-rock) — bedding (internal sediments)

g hemimorphite — smithsonite — sphalerite — 1 cm

h "Red ore" — smithsonite-Fe oxides — 5 cm
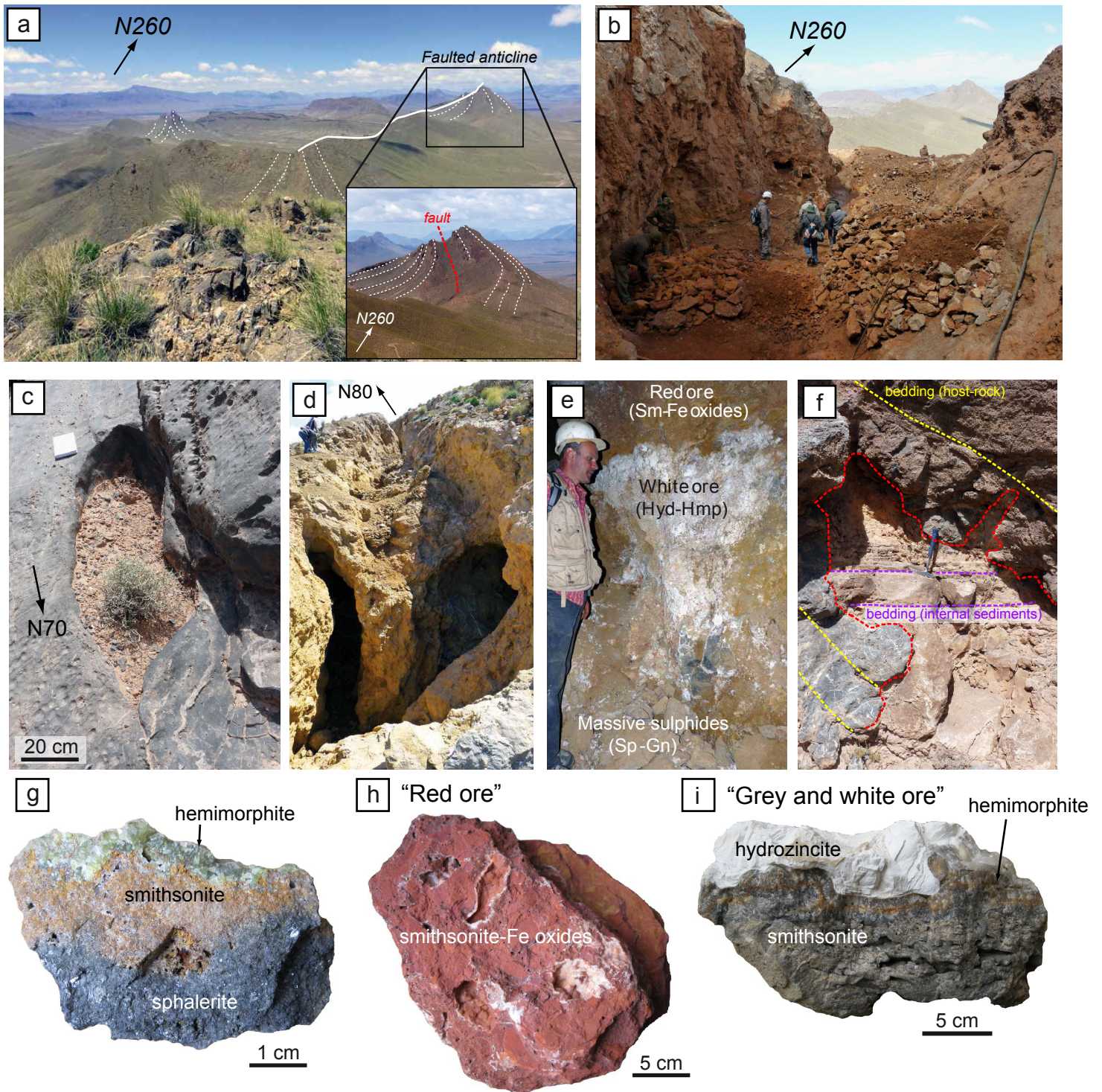
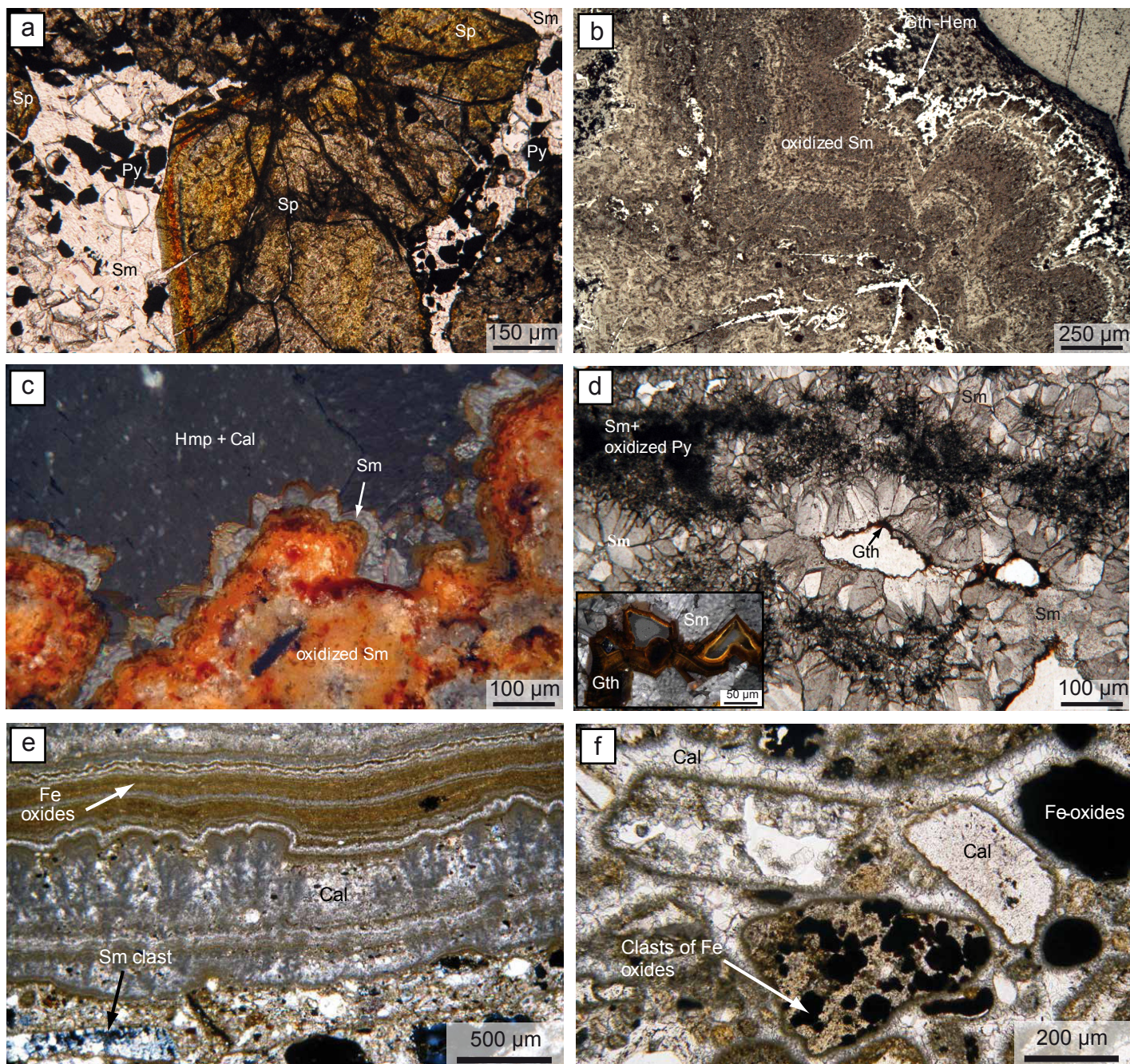**i** "Grey and white ore" — hydrozincite — smithsonite — hemimorphite — 5 cm
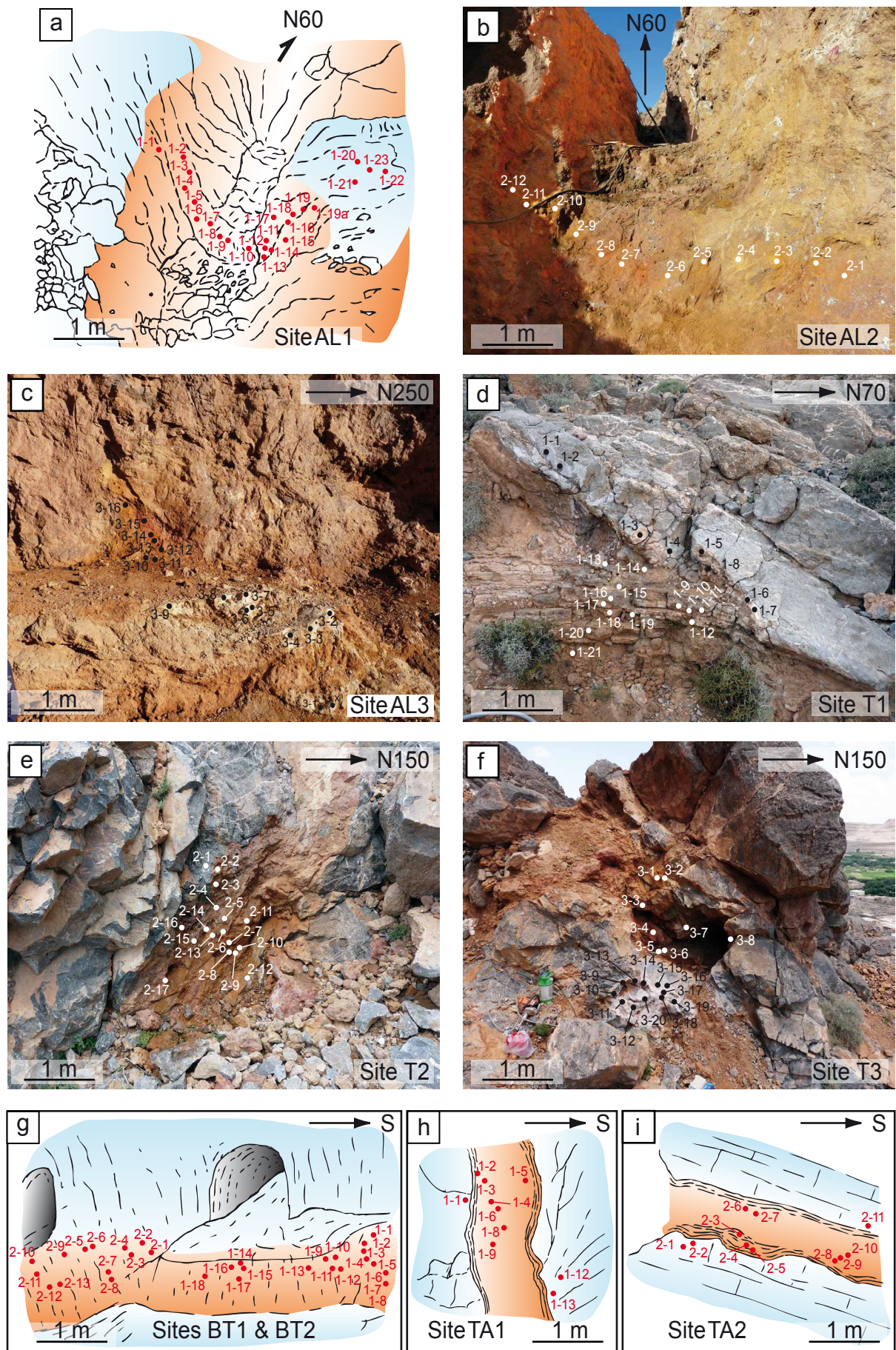
Figure 2

Figure 3

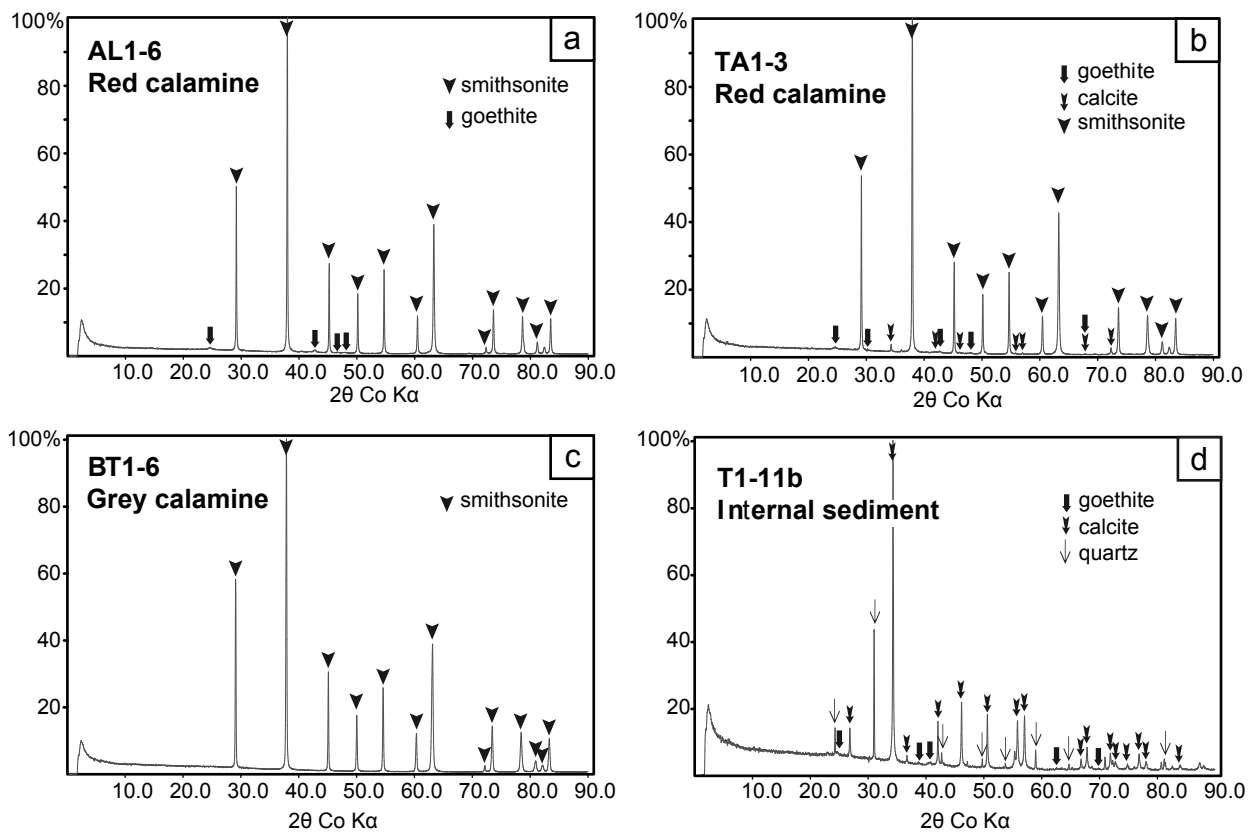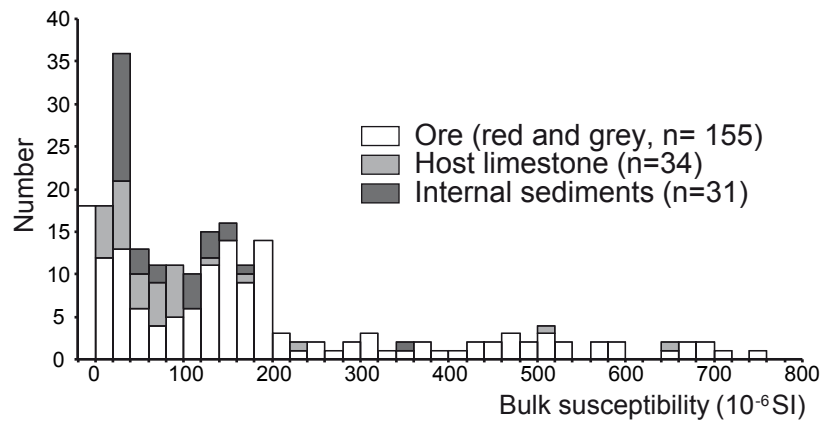Figure 3

Figure 4
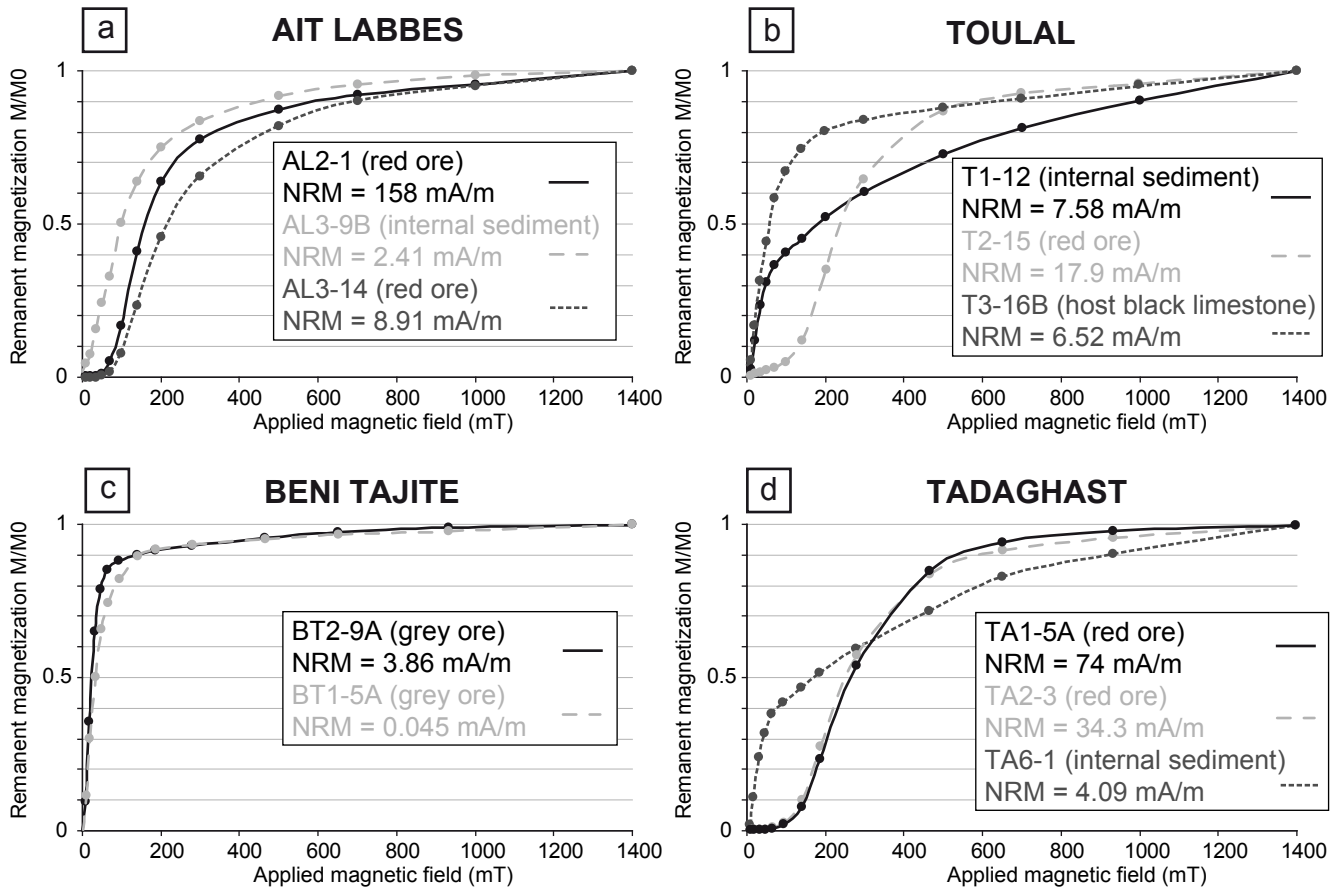

Figure 4

Figure 5

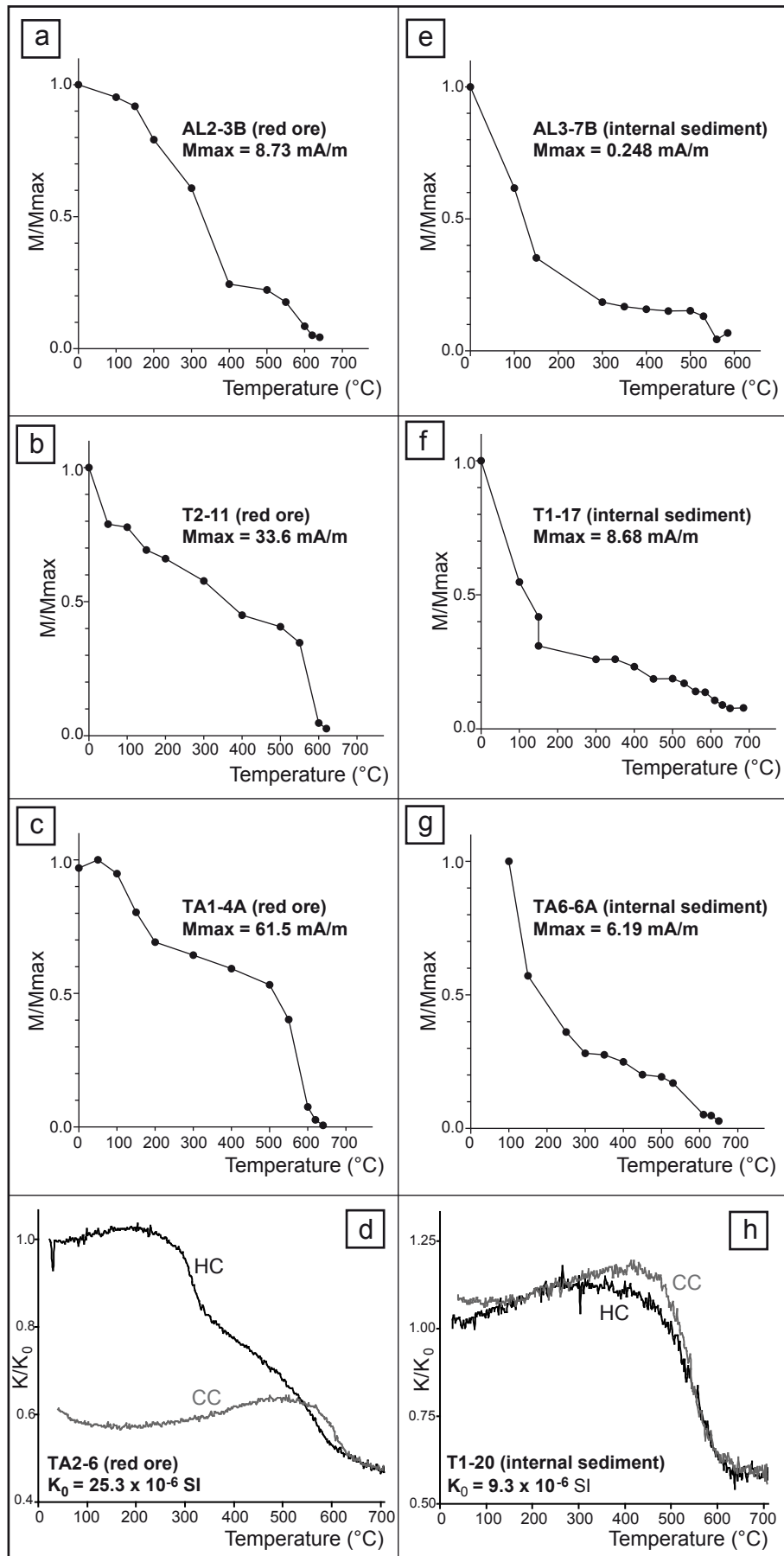Figure 5

Figure 6

Figure 6

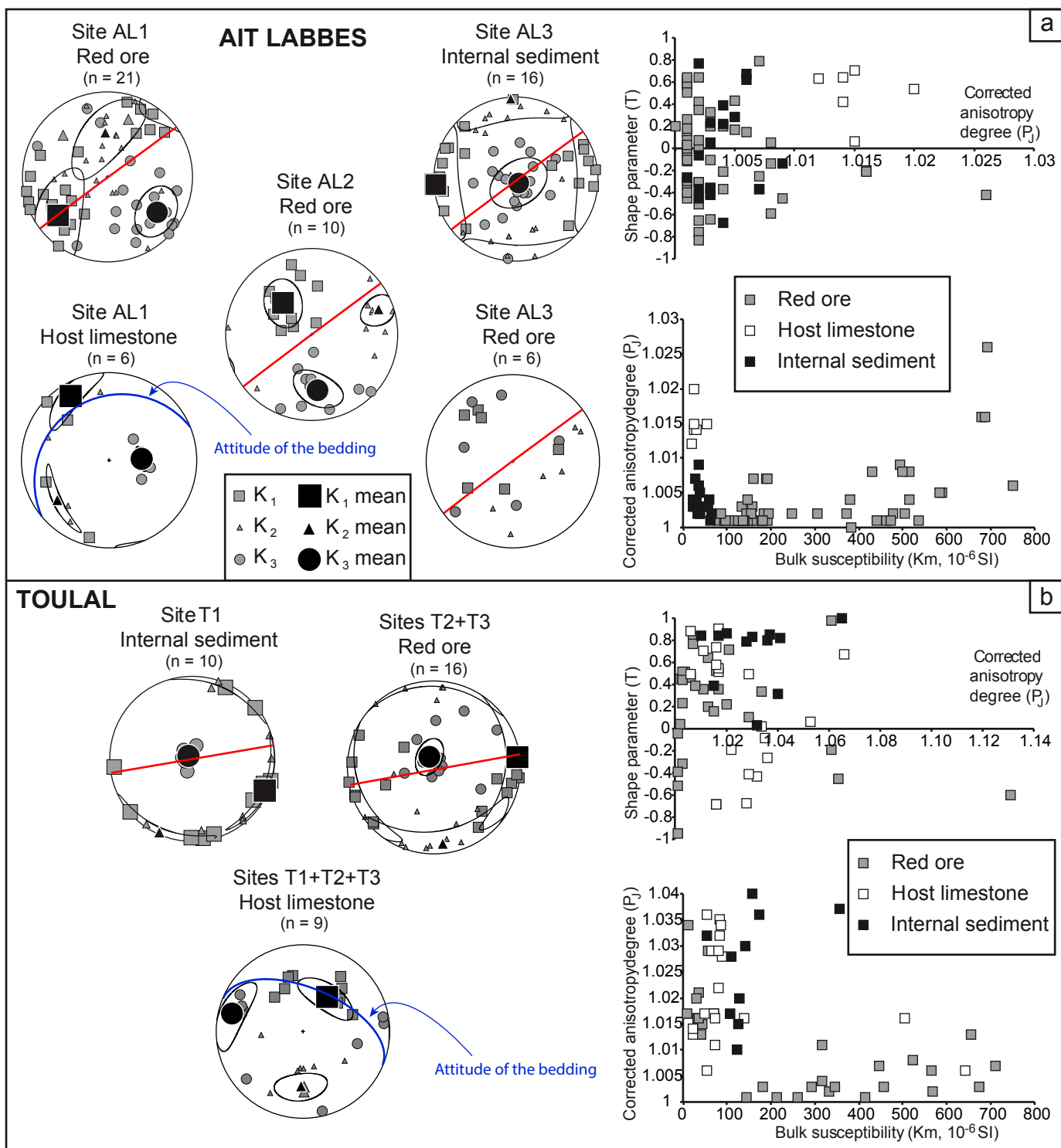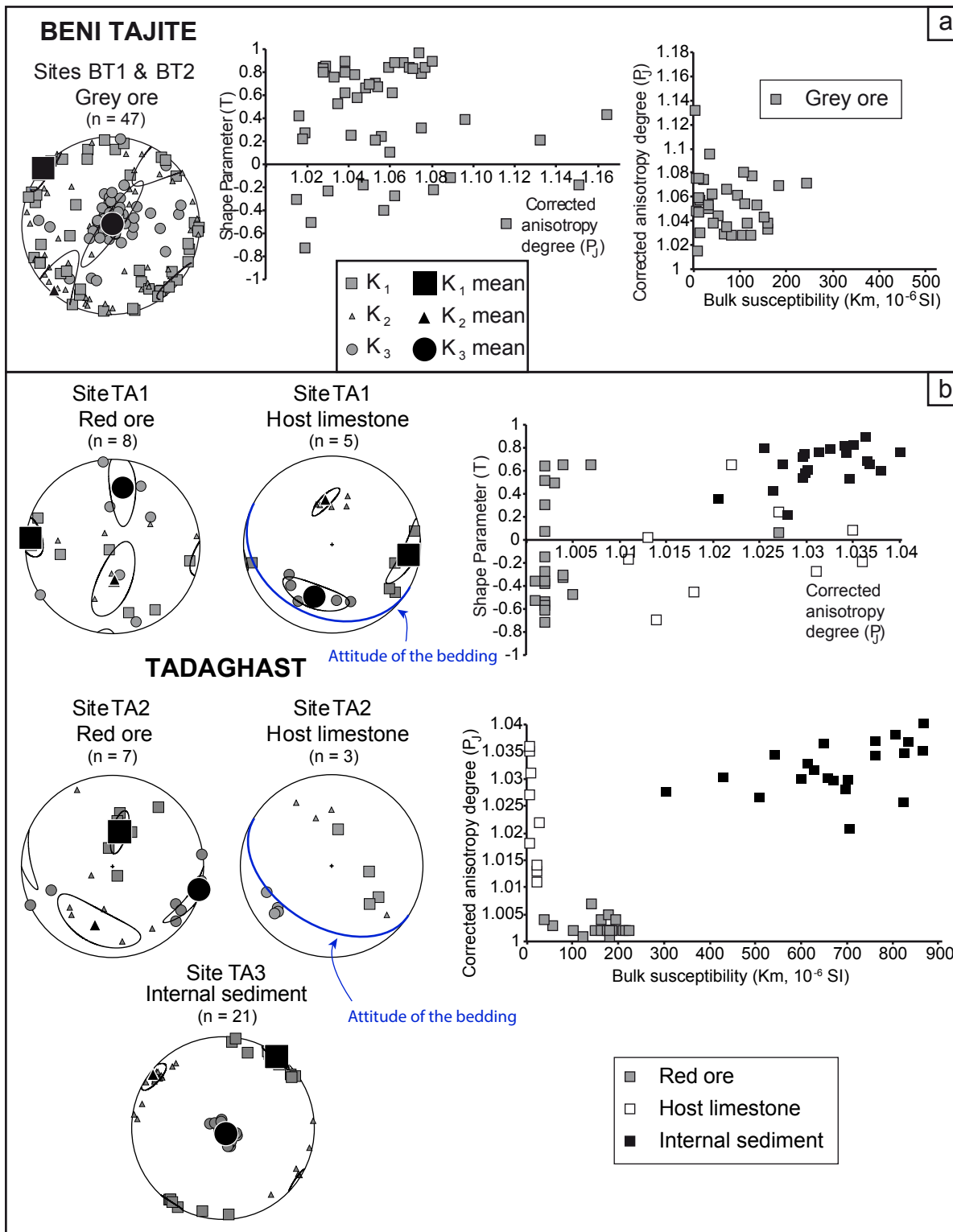Figure 7
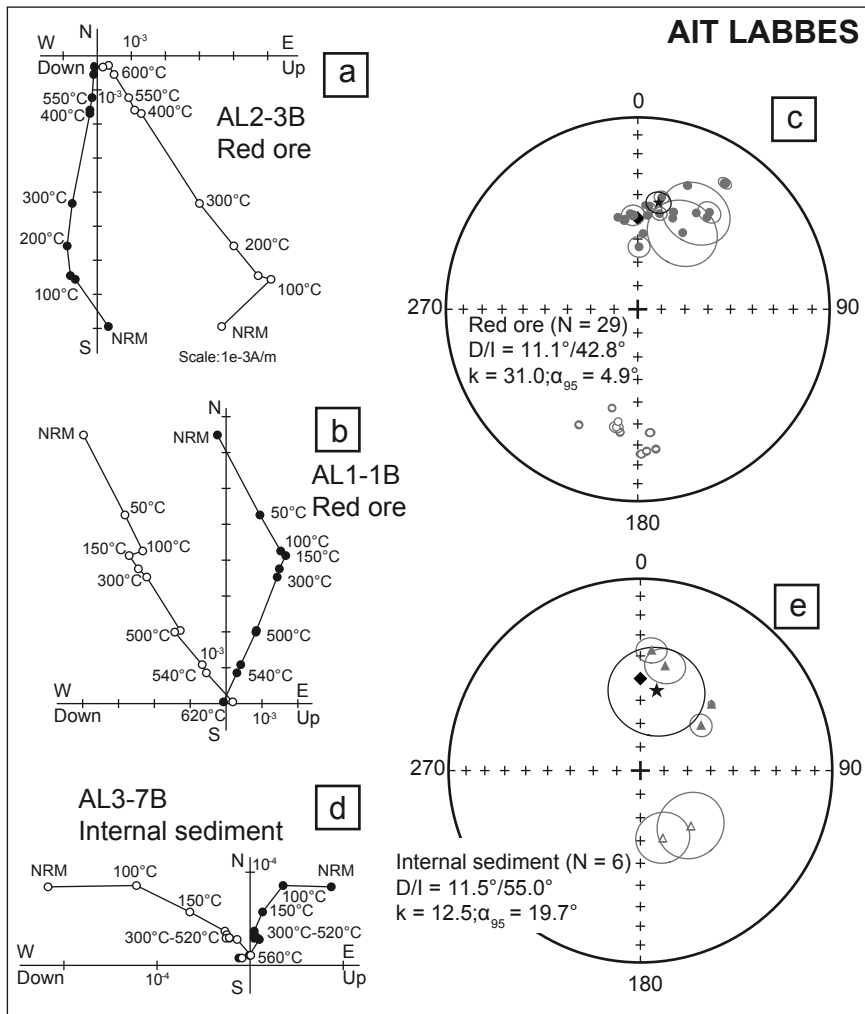

Figure 7

Figure 8
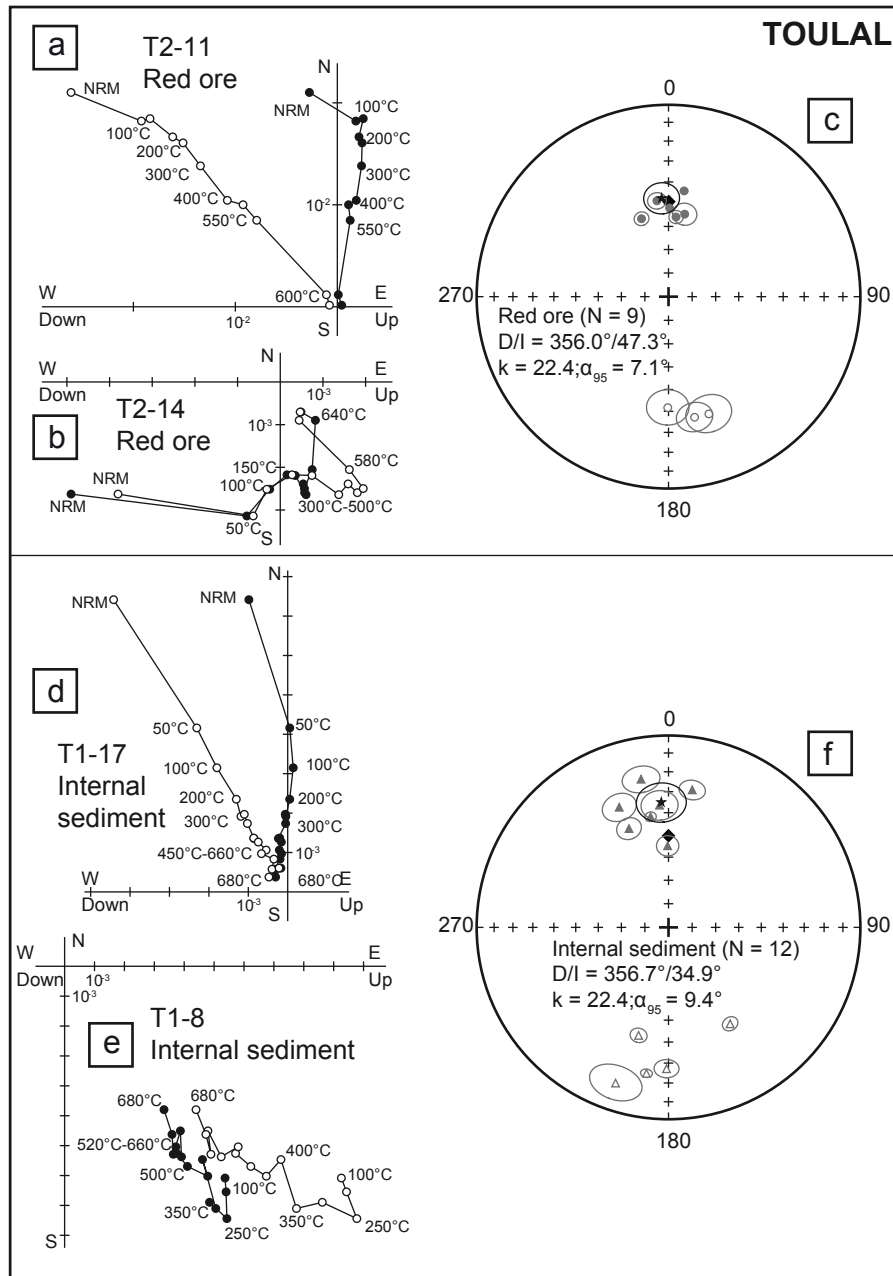

Figure 8

Figure 9

Figure 9

Figure 10

Figure 10

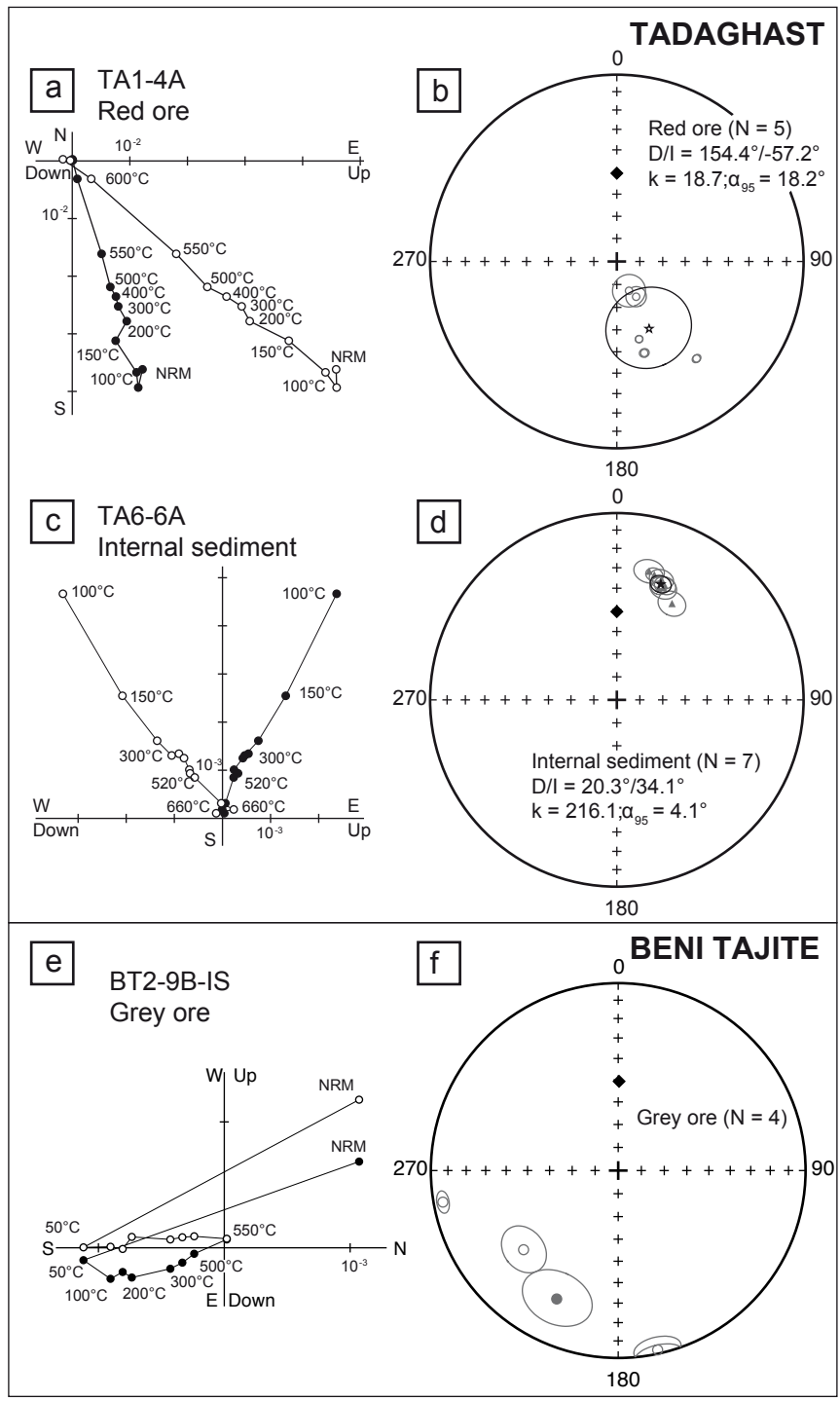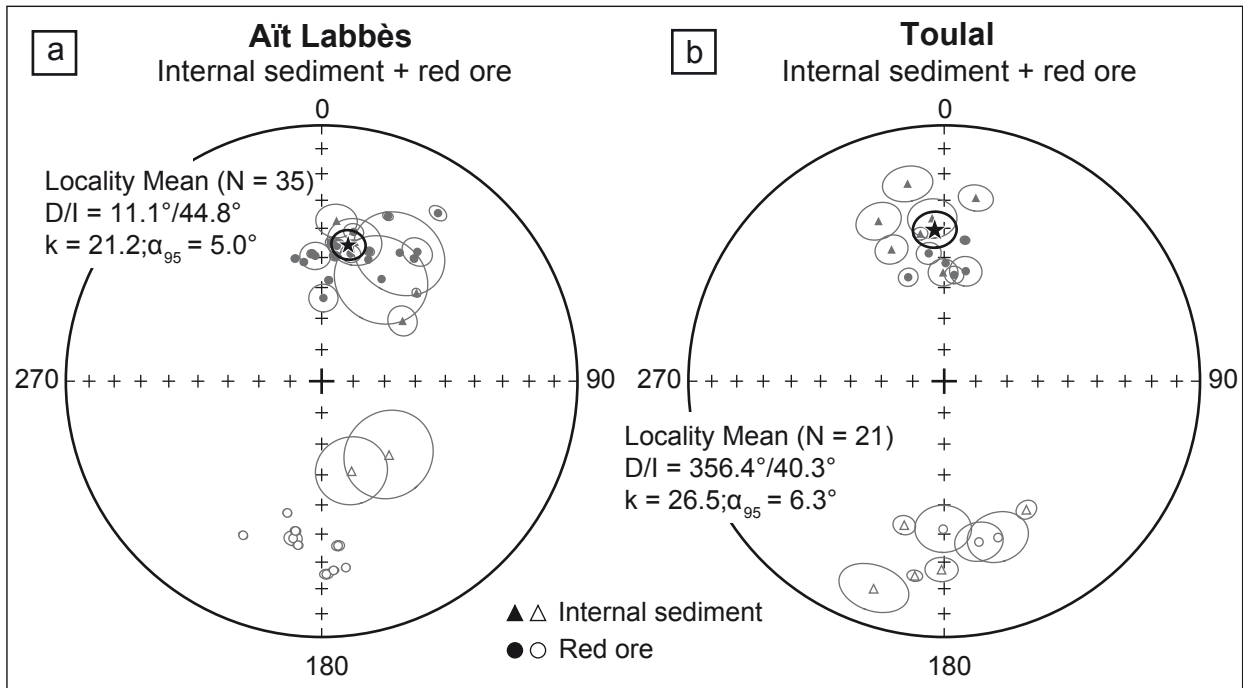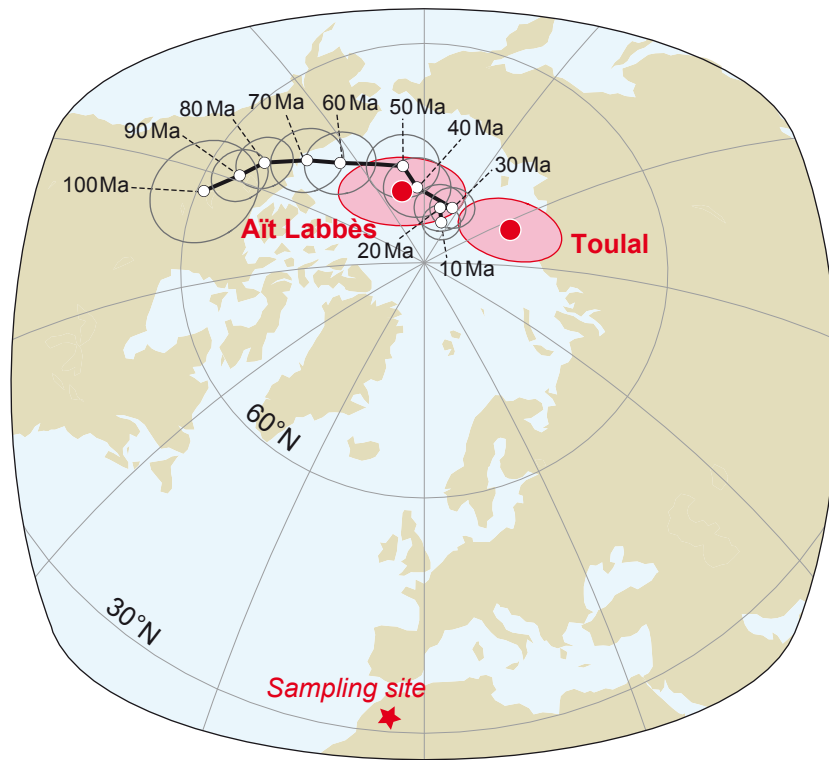Figure 11

Figure 11

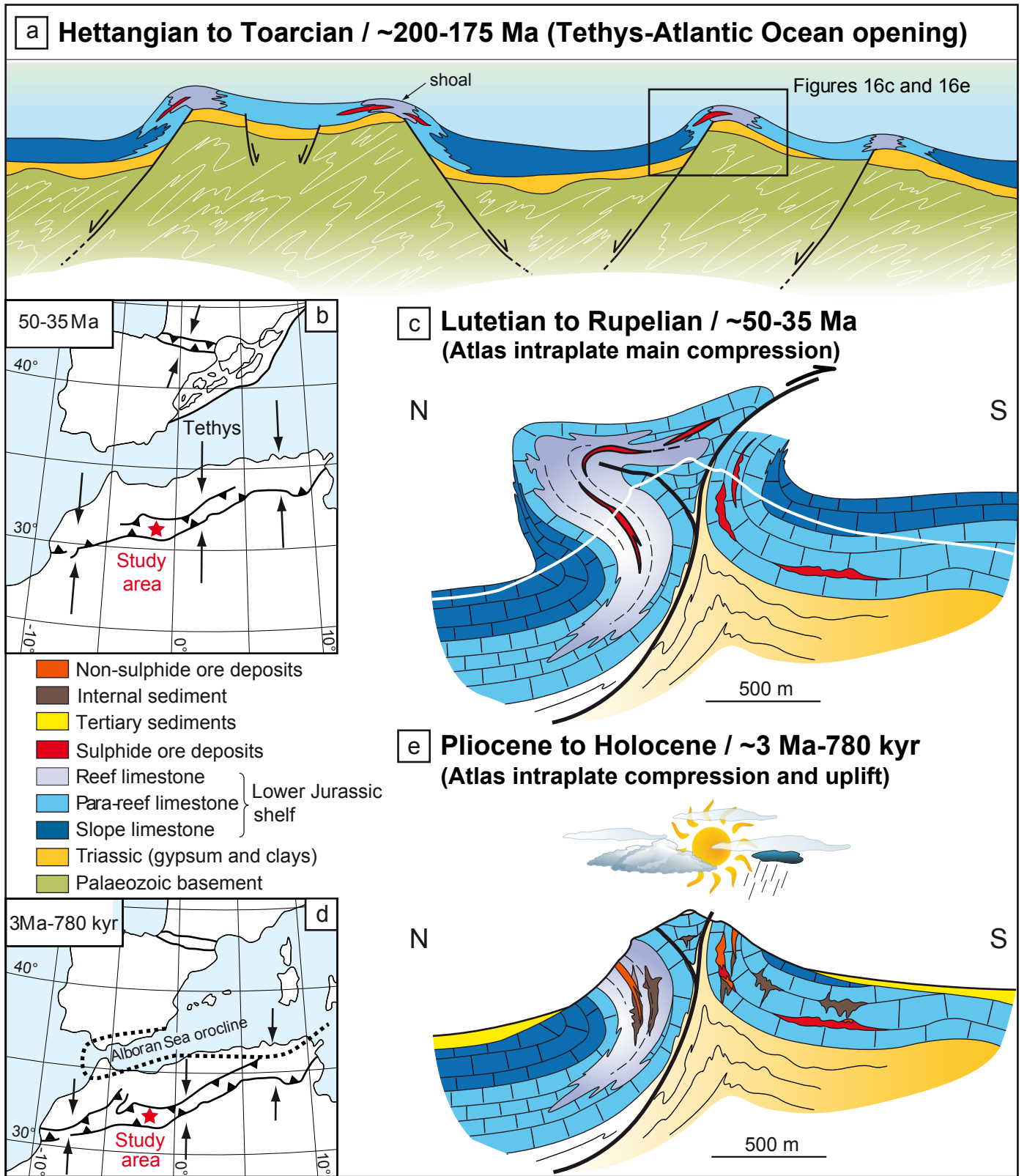Figure 12

Figure 12

Figure 13

Figure 13

Figure 14

Figure 14

Figure 15

Figure 15

Figure 16

Table 1

Table 1

Deposit	n/N	Km (x10⁻⁶ SI)	P_J	T	K₁				K₂				K₃			
					D (°)	I (°)	α_{95max}	α_{95min}	D (°)	I (°)	α_{95max}	α_{95min}	D (°)	I (°)	α_{95max}	α_{95min}
Aït Labbès (N32.384°; W04.384°)																
AL1 - Red ore	21/26	13.5	1.001	0.051	232.1	27.1	49.2	20.9	357.0	48.2	49.4	21.5	125.5	29.1	23.1	21.0
AL1 - Host limestone	6/6	30.1	1.015	0.499	329.1	15.7	31.3	11.0	231.4	25.4	31.3	4.7	87.6	59.5	11.6	3.8
AL2 - Red ore	10/18	561.0	1.009	-0.183	317.8	48.9	24.6	17.1	70.4	18.6	21.2	11.0	174.1	35.1	25.2	15.2
AL3 - Internal sediment	16/19	40.1	1.004	-0.059	80.5	4.7	37.9	20.5	350.3	2.6	39.6	20.3	231.9	84.6	25.1	20.6
AL3 - Red ore	6(N)	*no calculation - scattered data*														
Toual (N32.305°; W03.986°)																
T1 - Internal sediment	30/31	291.0	1.026	0.743	282.0	1.9	68.3	8.3	12.0	0.0	68.3	8.1	102.8	88.1	9.5	8.2
T2+T3 - Red ore	16/22	314.0	1.006	0.301	83.0	3.0	60.7	3.0	173.5	10.4	60.7	16.7	336.8	79.2	18.2	12.0
T1+T2+T3 - Host limestone	9/12	76.9	1.011	0.008	35.0	49.7	28.7	13.0	181.9	35.4	22.6	14.2	284.2	16.7	29.8	14.4
Beni Tajite (N32.302°; W03.451°)																
BT1/BT2 - Grey ore	47/49	49.3	1.035	0.391	310.8	0.1	18.6	9.4	220.8	2.2	48.9	12.7	44.0	87.8	48.4	8.4
Tadaghast (N31.636°; W06.606°)																
TA1 - Red ore	8/10	161.0	1.003	-0.361	276.0	5.8	17.4	10.9	177.0	57.3	37.8	15.0	9.6	32.1	37.3	10.6
TA1 - Host limestone	5/5	6.7	1.029	-0.109	97.7	13.9	28.5	7.8	351.3	48.9	17.2	4.9	198.8	37.8	29.4	12.2
TA2 - Red ore	7/11	180.0	1.002	-0.283	11.6	58.1	20.7	6.3	196.3	31.8	37.4	16.6	105.0	2.1	36.1	6.2
TA2 - Host limestone	3(N)	*no calculation - not enough data*														
TA3 - Internal sediment	21/21	695.0	1.033	0.641	36.8	2.4	11.4	3.7	306.6	5.1	11.4	8.2	152.0	84.4	8.7	4.1

Table 2

Site	n	D [°]	I [°]	MAD [°]
AIT LABBES				
Red ore				
AL1-12	9	34.7	21.2	2.5
AL1-14	9	1.2	63.4	4.5
AL1-1B	8	21.9	31.1	1.5
AL1-21A	4	30.4	51.8	14.4
AL1-4A	9	6.6	44.8	.0
AL1-4A	11	357.1	49.4	4.6
AL1-6A	8	21.0	47.8	.1
AL1-6A	10	12.8	47.6	3.0
AL2-12B	8	31.3	40.9	13.8
AL2-3B	8	178.6	-25.5	1.8
AL2-3B	9	188.2	-35.5	1.4
AL2-4B	10	190.3	-37.6	2.6
AL2-7	9	189.9	-40.3	1.5
AL2-7	10	194.6	-45.8	1.3
AL2-8B	8	37.0	39.8	1.1
AL2-8B	4	36.5	37.2	4.6
AL1-11	11	20.2	45.1	1.5
AL1-13A	10	6.0	49.3	1.6
AL1-13B	9	6.4	45.8	2.5
AL1-15B	9	4.0	57.5	1.2
AL1-5A	10	351.5	51.1	1.1
AL1-5B	10	347.8	49.4	1.2
AL1-6B	9	355.5	48.6	1.4
AL1-7	4	12.1	40.1	2.9
AL2-10A	10	3.9	44.7	1.7
AL2-10B	6	176.4	-26.8	1.4
AL2-2	9	207.0	-32.9	1.3
AL2-3A	6	174.3	-35.6	1.8
AL2-4A	3	172.6	-27.4	1.2
Mean	**N = 29; D/I = 11.1°/42.8°; k = 31.0; a₉₅ = 4.9°**			
Internal sediment				
AL3-1A	7	47.0	48.0	1.4
AL3-5B	5	161.6	-59.6	11.1
AL3-6A	8	53.3	57.6	4.7
AL3-6C	4	137.6	-57.9	14.1
AL3-7A	8	5.3	37.1	5.9
AL3-7B	8	13.3	43.3	8.0
Mean	**N = 6; D/I = 11.5°/55.0°; k = 12.5; a₉₅ = 19.7°**			

Site	n	D [°]	I [°]	MAD [°]
BENi TAJITE				
Grey ore				
BT1-11A	6	230.1	-34.5	9.8

Site	n	D [°]	I [°]	MAD [°]
TOULAL				
Red ore				
T2-1	15	353.1	48.3	3.7
T2-11	8	8.4	43.6	1.4
T2-13A	7	11.1	53.9	4.9
T2-13B	10	340.9	54.6	3.0
T2-14	4	161.0	-35.6	8.8
T2-14	4	180.4	-41.7	8.2
T2-4	5	.7	51.9	.7
T2-5	2	167.8	-35.9	6.9
T2-7	7	5.4	55.7	2.9
Mean	**N = 9; D/I = 356.0°/47.3°; k = 54.0; a₉₅ = 7.1°**			
Internal sediment				
T3-15A	7	349.5	22.5	6.7
T3-3B	9	359.4	55.0	4.5
T3-4A	11	355.8	36.3	7.0
T3-2A	4	338.2	43.8	4.9
T3-4A	10	180.8	-27.2	4.5
T3-5A	8	337.7	32.8	6.5
T3-6B	8	198.8	-15.4	9.1
T1-17	10	9.8	28.1	4.8
T1-6A	10	188.6	-24.1	2.1
T1-7A	8	195.5	-41.2	3.3
T1-8	10	147.4	-40.1	3.1
T1-9	8	350.8	41.2	2.2
Mean	**N = 12; D/I = 356.7°/34.9°; k = 22.4; a₉₅ = 9.4°**			
TADAGHAST				
Red ore				
TA1-2A	6	151.3	-72.5	4.4
TA1-2B	8	157.4	-76.2	7.1
TA1-3	7	140.6	-33.2	1.8
TA1-4A	9	163.3	-47.6	2.0
TA1-4B	10	164.0	-54.4	1.6
Mean	**N = 5; D/I = 154.4°/-57.2°; k = 18.7; a₉₅ = 18.2°**			
Internal sediment				
TA6-2A	10	29.8	40.3	5.7
TA6-3A	8	20.4	36.4	2.9
TA6-3B	5	16.7	30.7	3.3
TA6-4B	10	20.3	31.7	4.7
TA6-5B	10	22.9	34.0	4.2
TA6-6A	9	22.5	35.3	5.3
TA6-7A	10	14.1	29.7	5.8
Mean	**N = 7; D/I = 20.3°/34.1°; k = 216.1; a₉₅ = 4.1°**			